Article

New Tilt Fractional-Order Integral Derivative with Fractional Filter (TFOIDFF) Controller with Artificial Hummingbird Optimizer for LFC in Renewable Energy Power Grids

Emad A. Mohamed [1,2,†] , Mokhtar Aly [3,*,†] and Masayuki Watanabe [2,†]

1 Department of Electrical Engineering, Aswan University, Aswan 81542, Egypt
2 Department of Electrical and Electronic Engineering, Kyushu Institute of Technology, Kitakyushu 804-8550, Fukuoka, Japan
3 Facultad de Ingeniería, Arquitectura y Diseño, Universidad San Sebastián, Bellavista 7, Santiago 8420000, Chile
* Correspondence: mokhtar.aly@uss.cl
† These authors contributed equally to this work.

Abstract: Recent advancements in renewable generation resources and their vast implementation in power sectors have posed serious challenges regarding their operation, protection, and control. Maintaining operating frequency at its nominal value and reducing tie-line power deviations represent crucial factors for these advancements due to continuous reduction of power system inertia. In this paper, a new modified load frequency controller (LFC) method is proposed based on fractional calculus combinations. The tilt fractional-order integral-derivative with fractional-filter (TFOIDFF) is proposed in this paper for LFC applications. The proposed TFOIDFF controller combines the benefits of tilt, FOPID, and fractional filter regulators. Furthermore, a new application is introduced based on the recently presented artificial hummingbird optimizer algorithm (AHA) for simultaneous optimization of the proposed TFOIDFF parameters in the studied two-area power grids. The contribution of electric vehicle (EVs) is considered in the centralized control strategy using the proposed TFOIDFF controller. The performance of the proposed TFOIDFF controller has been compared with the existing tilt with filter, PID with filter, FOPID with filter and hybrid fractional-order with filter LFCs from the literature. Moreover, the AHA optimizer results are compared with the featured LFC optimization algorithms in the literature. The proposed TFOIDFF and AHA optimizer are validated against renewable energy fluctuations, load stepping, generation/loading uncertainty, and power-grid parameter uncertainty. The AHA optimizer is compared with the widely-used optimizers in the literature, including the PSO, ABC, BOA, and AEO optimizers at the IAE, ISE, ITAE, and ITSE objectives. For instance, the proposed AHA method has a minimized IAE after 34 iterations of 0.03178 compared to 0.03896 with PSO, 0.04548 with AEO, 0.04812 with BOA, and 0.05483 with ABC optimizer. Therefore, fast and better minimization of objective functions are achieved using the proposed AHA method.

Keywords: artificial hummingbird algorithm (AHA); fractional-order controller; frequency stability; load frequency control; renewable energy power grids

MSC: 68N30, 49M99

1. Introduction

For decades, electrical power has provided vital contributions in technological advancements and developments. A rising population and concurrent technological progress have lead to tremendous increases in load demand. In the past, traditional non-renewable resources dominated installations in the energy sector. However, due to their scarcity and their adverse environmental impacts, concerns are deviating towards sources of power

through installing renewable energy-based sources (RESs) [1]. Therefore, more focus on sustainable development is required based on replacing non-renewable sources with RESs, including wind generation, solar photovoltaic (PV) generation, bio-diesel, etc. Additionally, enhancing RES-based power grids by using energy storage devices, cooperative operation of installed electric vehicles (EVs), etc., have attracted important attention from researchers, industry, and governmental regulations and incentives. They can help at preserving the resiliency and reliability of power grids [2]. Additionally, performance enhancement of power grids can be achieved through employing recent single- and multi-objective optimization algorithms, including the robust optimization methods [3], and the stochastic optimization methods [4].

RES-based power grids face several challenges, such as intermittency, inconstant loading profiles, reduced inertia, etc. The interconnection of RES-based power grids is fruitful in several aspects. However, RESs introduce weak power grids with unstable response to disturbance [5]. The weak inertial response is the principal cause of power grid instability compared with non-renewable-based traditional grids. The coupling of PV and wind generations with power interfacing converters renders them incapable of bearing a significant inertial-response, which limits their capability for balancing power demands [6]. With increased penetration level of RESs, a low inertial response leads to severe unstable power grids and reduced controllability of frequency deviations in RES-based power grids [7].

1.1. Literature Survey

The introduction of advanced and optimized control methods can lead to better performing RES-based power grids [8,9]. The load frequency controller (LFC) has been vastly introduced to solve the frequency deviation problems of RES-based power grids. LFCs are responsible for the regulation of generated power to achieve the mitigation of loading variations, inconstant parameters, fluctuating nature of RESs, disturbances, etc., [10]. The type of applied LFC method determines the performance of power grids against disturbances. In addition, proper optimum LFC design methodology determines the power grid response and the complexity of design process [11].

Several LFC solutions have been introduced in the literature, such as the sliding mode [12], model predictive [13,14], deep learning [15], linear matrix inequality [16], robust control [17,18], fuzzy logic [19], internal model [20], intelligent control [21], data-driven [22], etc., control methodologies. Several reviews and comparison papers exist in the literature for LFC methods [11,23,24]. The recent intelligent LFC strategies have proven successful in the handling of frequency stability issues. However, they possess several limitations, such as requirement of high computational complexities, and/or huge amount of data for the training process, and/or powerful processors required for implementation, etc. Meanwhile, integer-order (IO) and fractional-order (FO) traditional controllers are still receiving wide attention and developments for LFC in single and multi-area regulated/deregulated power grids [25]. Moreover, centralized/decentralized single/cascaded structures have been presented in the literature, in which, optimized design and optimizer algorithms have shown notable effects on power grid response at disturbance actions [26].

The main elements in IO- and FO-based LFC are the proportional (P), derivative (D), integral (I), tilt (T), filter (F) gains, FO operators, etc. The IO integral (I) has found widespread employment in the literature and several optimizers have been introduced for its design optimization. The design of PID LFC parameters using the stability boundary-locus (SBL) was presented in [27], and the Artificial-Bee Colony (ABC) was used in [28]. The PI LFC was proposed in [29] using the Harris Hawks optimizer (HHO). An Adaptive integrator LFC with the elder-scrolls online (ESO) and balloon-effect modulation (BE) was proposed in [30] for mitigating parameter uncertainty problems. The IO-based LFC is simple, and low-complexity in design, and implementation. However, they are not able to perfectly mitigate the existing fluctuations and disturbances in RES-based power grids. Furthermore, several LFC methods have been presented in the literature using the PIDF in [31,32], the

two degree-of-freedom (2DoF) PID (2DoF-PID) in [33], the cascaded PD and PID in [34], the PID with a second-order derivative (PID2D) in [35], the fuzzy logic control (FLC) with PID (FLC-PID) in [36], and the neuro-fuzzy LFC in [37]. From another viewpoint, the PI and PID with slap swarm optimization algorithm (SSA) was presented in [38] with a real-time price-based demand response method. A 2DoF-PID was proposed in [39] and optimized by the flower pollination optimizer algorithm (FPA). The controller was compared with the classical PI, PID, and 2DoF PI controller, and demonstrated superior performance.

Moreover, several proposals have been presented in the literature for using the FO-based LFC [40]. The FOPID LFC with the movable damped-wave optimizer (MDWA) was provided in [41] for multi-area grids. An optimized FOPID using sine cosine algorithm (SCA) was presented in [42]. In [43], cascaded structure of FO-IDF was proposed. Furthermore, the TID LFC has been proposed with different structures in the literature [44]. Optimized TID LFC has been introduced based on artificial-bee colony (ABC) algorithm for EV power grids in [45]. Another pathfinder algorithm (PFA)-based optimized TID LFC was proposed in [46]. In [47], the TIDF LFC was optimized based on the differential evolution algorithm (DE). Additionally, the PI-TDF LFC with the slap swarm algorithm (SSA) was proposed in [48].

A modified-FO hybrid structure based on TID and FOPID control was presented in the literature for two-area power grids in [2]. Optimized design of the presented controller is achieved using the artificial ecosystem optimizer (AEO). The dual stage LFCs optimized by butterfly optimization algorithm (BOA) have been presented in [49]. A hybrid FO LFC method (namely FOTID) optimized by manta-ray foraging optimization (MRFO) was proposed in [50]. Series of combined and cascaded structures have also been presented in the literature. A cascaded FOPID with FLC with the imperialist competitive-optimizer algorithm (ICA) was provided in [51]. Further combined fuzzy and FO LFC methods were provided in [52] using the FLC-FOPI-FOPD, in [53] using FL-FOPIDF, and in [54] using the FLC-PIDF-FOI. Moreover, an improved ICA-optimized FPIDN-FOPIDN LFC method was proposed in [43] for two-area grids.

1.2. Motivation

It has become clear that several LFC proposals exist in the literature with various optimization methods. The combination of LFC-type with the selected optimizer determines to a large extent the power grid performance during transients. However, enhanced performance of LFC methods and design strategies are needed for mitigating the expected loading effects of RESs in future low-inertial grids. Accordingly, this paper presents a combined tilt, FOPID, and fractional filter regulators for developing a new modified FO LFC scheme.

From another perspective, massive tuning efforts are needed for their parameters. Several metaheuristic optimizers methods lack reliability as a result of their increased probability for settling at local minimums [55]. Moreover, proper tuning is required for several parameters, especially for FO-based LFC methods. Therefore, great concerns exist regarding the determination of parameter optimization [56]. Additionally, some optimizers suffer from longer elapsed time, saturation, and high sensitivity to parameter variations. Another issue of some optimizers is the long computational time and hence frequent iterations are needed for assuring solution convergence.

The recently presented artificial hummingbird optimizer algorithm (AHA) represents a new, effective, and bio-inspired optimization algorithm [57]. It simulates the behavior of special flight skill, and the intelligent strategies for foraging of hummingbirds. It has shown improved performance in optimum allocation of RESs [58] and energy management of RES-based microgrid systems [59]. The main differences of AHA that result in its superiority are summarized as follows [57]:

1. The AHA employs a different biological background compared to other existing metaheuristic optimization algorithms. The AHA optimizer employs three different foraging strategies with three various flight skills inspired by the hummingbird.

2. The AHA optimizer uses different strategies for the exploration, and the exploitation stages. The migration foraging strategy of the AHA optimizer guarantees exploration stage in search space. Whereas, the exploitation stage is promoted through the territorial-foraging strategy. In addition, the guided-foraging strategy emphasizes the exploration stage during early stages, and highlights the exploitation stage during later stages.

3. The AHA optimizer has its own distinct mechanism of memory updating. Each one of the hummingbirds needs to know the last visit time to other hummingbirds. The visit time information is recorded within the visit table, wherein each one of the hummingbirds can select its desired source of food.

Consequently, based on the aforementioned factors, the AHA optimizer possesses three significant differences compared to the existing optimization algorithms. The AHA optimizer mimics the food searching behaviors of hummingbirds using three different foraging strategies, in addition to the superior memories of hummingbirds and their impressive skills of flight. Thus, the AHA optimizer is selected in this paper for optimizing the proposed controller's parameters and is compared with different existing optimization algorithms in the literature.

1.3. Contribution

Motivated by the previous discussions, the main contributions in this paper are summarized as follows:

- A new modified load frequency controller (LFC) based on combining the tilt, FOPID, and fractional filter regulators, namely the tilt FO integral-derivative with fractional-filter (TFOIDFF) controller. The combination of three efficient regulators improves the stability performance, fast transients, and mitigation of existing RESs and loading fluctuations.
- A new controller optimization application for the proposed TFOIDFF controller is proposed based on the newly presented bio-inspired artificial hummingbird optimizer algorithm (AHA). The proposed AHA-based optimization process can eliminate the massive training data required and/or complicated mathematical calculations that are required in other methods.
- A decentralized EV controller using the proposed TFOIDFF LFC controller is proposed in this paper. The TFOIDFF achieves both the LFC functionality and EV control functionality.
- Simultaneous determination of optimum proposed TFOIDFF LFC parameters with AHA optimizer is presented in this paper. All the parameters in interconnected power grids are determined jointly to address the objective function that represents the mitigation of existing frequency and tie-line power deviations in the interconnected power grids.

The rest of the paper is organized as follows: Mathematical models of the studied RES-based interconnected power grids with state-space representation are presented in Section 2. The existing LFC and proposed TFOIDFF controller are detailed in Section 3. The principles of the AHA optimizer and the proposed optimization method are presented in Section 4. A performance validation of the proposed TFOIDFF controller and AHA optimizer is provided in Section 5. Lastly, the paper is concluded in Section 6.

2. Mathematical Models of Interconnected Power Grids with EVs

2.1. Power Grid Structure

A two-area interconnected power grid case study from [2,50] is used for validating the new proposed TFOIDFF and AHA-optimizer-based controller. The structure and components of interconnected power grids with installed EV systems are shown in Figure 1. The power grid is divided into two areas (area *a* and area *b*). Area *a* contains thermal energy generation, local loads, and wind RES plant. Whereas, area *b* contains hydraulic energy generation, local loads, and PV RES plant. It is assumed that the EVs are equally distributed among the interconnected power grids.
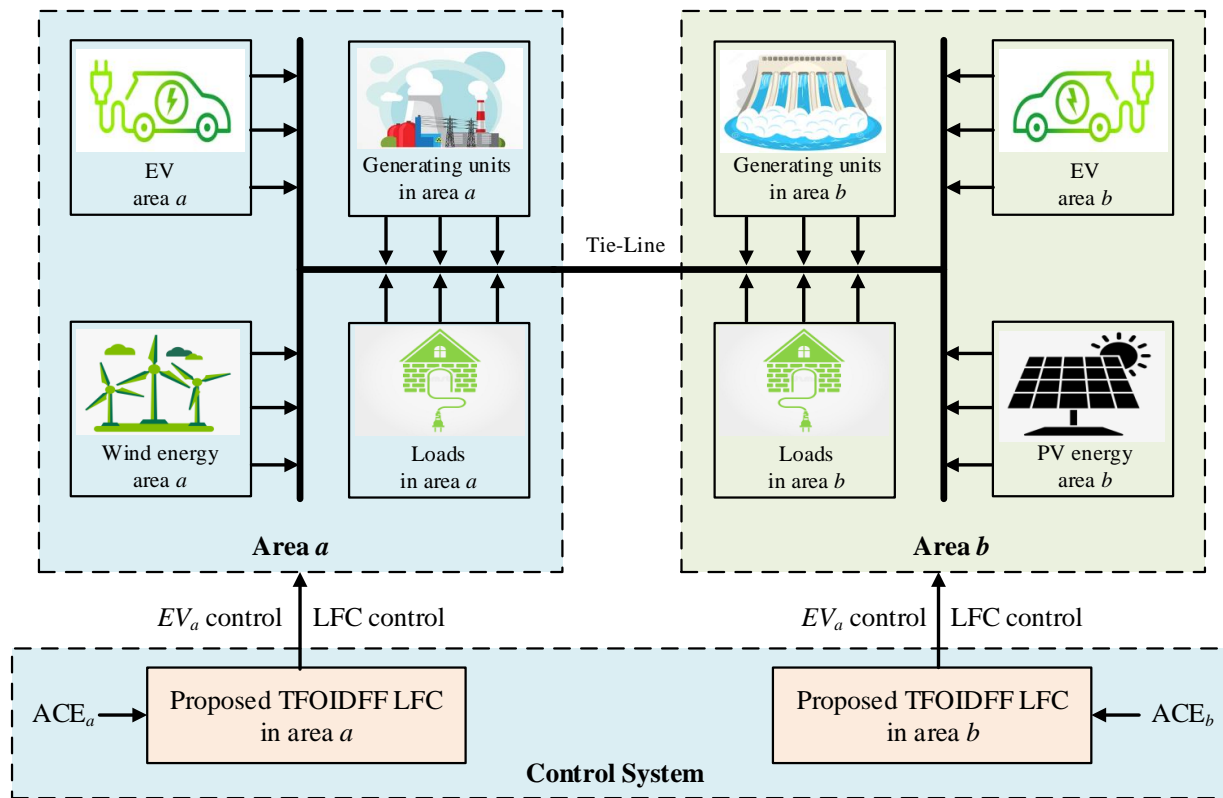
Figure 1. Structure of two-area power grid with EVs.

2.2. EV Modeling

With recent regulations and trends, installed EVs can effectively participate in frequency regulation function. Thus, the use of existing EV batteries can reduce the cost for installing new energy storage devices and control charging/discharging times of EVs [2]. To perform this added frequency regulation functionality, modeling of the internal battery characteristics is needed in the LFC model. It is assumed in this paper that EVs are equally distributed among interconnected power grids. The widely employed Thevenin equivalent model of EV systems is implemented in this paper as shown in Figure 2 and as described in [60,61].

The EV Thevenin equivalent-based model includes an open-circuit voltage source V_{oc}. The source V_{oc} is dependent on the current state-of-charge (SOC) of the EV battery ($V_{oc}(SOC)$ in the model). The model includes series resistance R_s and shunt RC circuit (R_t, C_t). The RC circuit models the transient overvoltage effects. The output terminal voltage of EVs is the difference between $V_{oc}(SOC)$ and voltage drops V_s and V_t as in Figure 2. The relation among the $V_{oc}(SOC)$ and SOC of installed EV batteries is represented by Nernst equations as follows [62]:

$$V_{oc}(SOC) = V_{nom} + S \, \frac{RT}{F} ln \left(\frac{SOC}{C_{nom} - SOC} \right) \tag{1}$$

where, V_{nom} is nominal voltage, and C_{nom} is the nominal capacity (in Ahr) of EV batteries. Whereas, S denotes the sensitivity parameter of $V_{oc}(SOC)$, F is Faraday's constant, T is the temperature, and R is the gas constant.
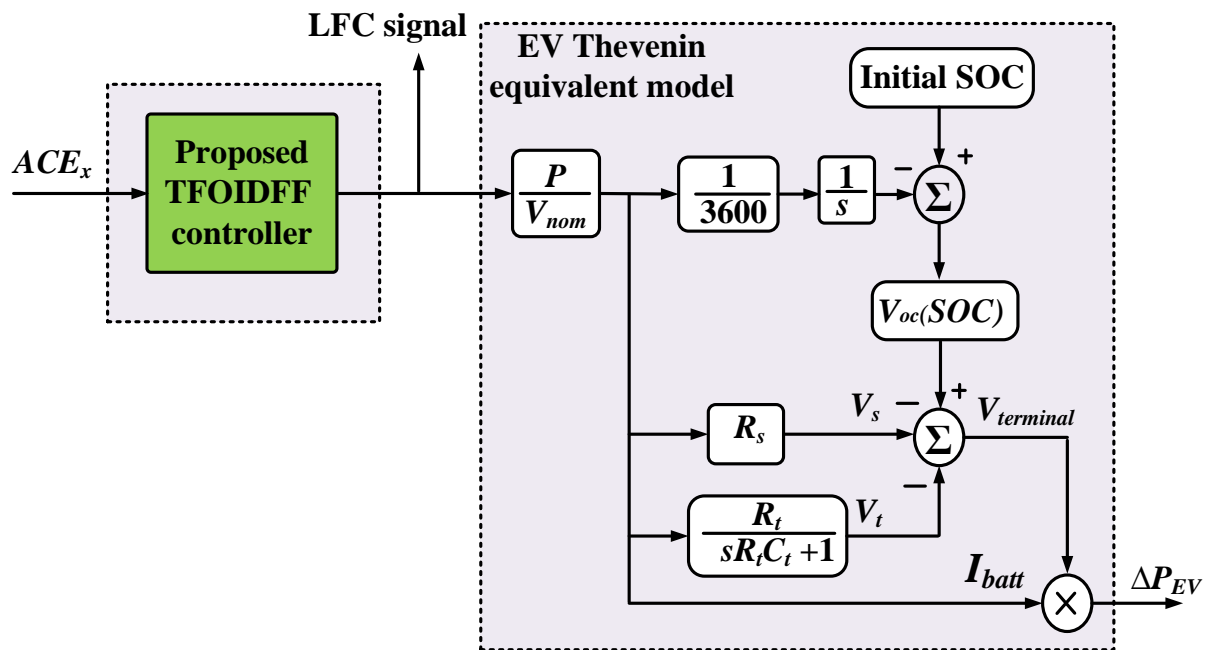
Figure 2. Thevenin equivalent model of EVs for frequency regulation.

2.3. Traditional Energy Source Models

The thermal energy generation exists in area *a*, and hydraulic energy exists in area *b*. The thermal plants are normally represented by governor $G_g(s)$ followed by turbine system $G_t(s)$. They are modeled as follows [63]:

$$G_g(s) = \frac{1}{T_g s + 1} \tag{2}$$

$$G_t(s) = \frac{1}{T_t s + 1} \tag{3}$$

where, T_g and T_t are the time constants for the governor and turbine system, respectively.

Additionally, hydraulic generation systems $G_h(s)$ are modeled as follows [50]:

$$G_h(s) = \frac{1}{T_1 s + 1} \cdot \frac{T_R s + 1}{T_2 s + 1} \cdot \frac{-T_w s + 1}{0.5 T_w s + 1} \tag{4}$$

where, T_1, T_R, T_2 are time constants representing governor, the transient droops, and reset-time of the hydraulic governor system, respectively. Whereas, T_w represents the starting time for the water penstocks.

2.4. RESs' Models

The wind energy system $G_{WT}(s)$ is expressed through the following model [64]:

$$G_{WT}(s) = \frac{K_{WT}}{T_{WT} s + 1} \tag{5}$$

where, K_{WT}, T_{WT} are wind plant's gain, and time constant, respectively. Whereas the model of the PV energy system $G_{PV}(s)$ is expressed as follows [64]:

$$G_{PV}(s) = \frac{K_{PV}}{T_{PV} s + 1} \tag{6}$$

where, K_{PV}, T_{PV} are the PV plant's gain, and time constant, respectively.

2.5. Complete System State-Space Model

The complete two-area power grid system modeling is shown in Figure 3 including various existing elements' models. The numerical values of the studied two-area power grid are tabulated in Table 1 using the system data from [50,61]. Normally, the state-space model is the most suitable way to linearize the two-area power grid. The general state-space model is represented as follows:

$$\dot{x} = Ax + B_1\omega + B_2u \tag{7}$$

$$y = Cx \tag{8}$$

where, x denotes the state variables representing vector, y denotes the output states representing vector, ω denotes the existing disturbance representations, and u is control representing vector.

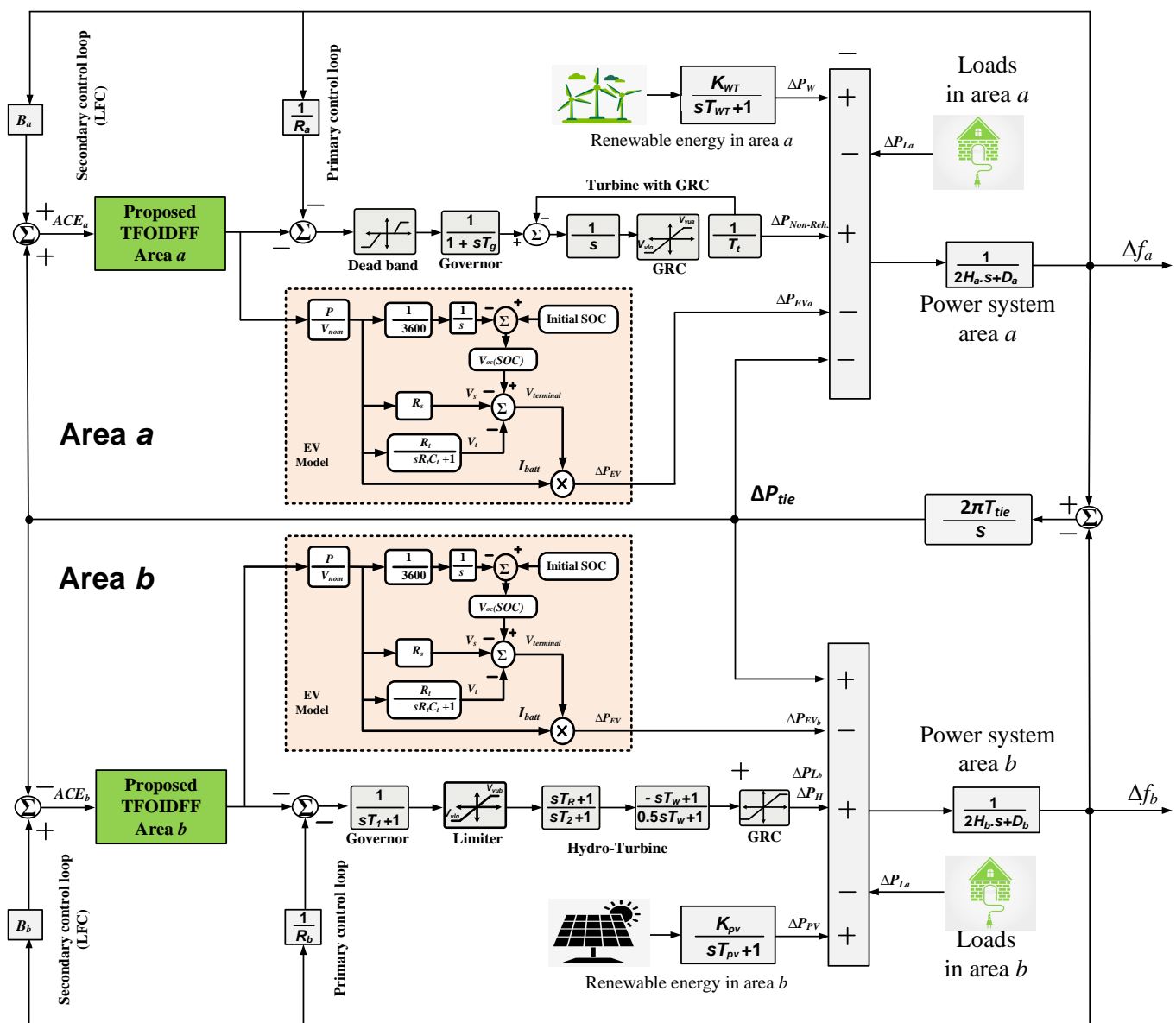**Figure 3.** Complete model for the studied two-area power grid system.

The representing vector x of state variables, and representing vector ω for disturbances are expressed as follows:

$$x = \begin{bmatrix} \Delta f_a & \Delta P_{ga} & \Delta P_{ga1} & \Delta P_{WT} & \Delta f_b & \Delta P_{gb} & \Delta P_{gb1} & \Delta P_{gb2} & \Delta P_{PV} & \Delta P_{tie,ab} \end{bmatrix}^T \quad (9)$$

$$\omega = \begin{bmatrix} \Delta P_{la} & P_{WT} & \Delta P_{lb} & P_{PV} \end{bmatrix}^T \quad (10)$$

In the proposed system, control variables are represented by ACE signals ($ACEo_a$ and $ACEo_b$) in the power grid system in addition to the supplied EVs' power (ΔP_{EVa} and ΔP_{EVb}). Therefore, the vector representing control variables is expressed by:

$$u = \begin{bmatrix} ACEo_a & \Delta P_{EV_a} & ACEo_b & \Delta P_{EV_b} \end{bmatrix}^T \quad (11)$$

In which, matrices A, B_1, B_2, and C are composed of power grid model parameters used for state-space representation. They are constructed for the studied power grid as follows:

$$A = \begin{bmatrix} -\frac{D_a}{2H_a} & \frac{1}{2H_a} & 0 & \frac{1}{2H_a} & 0 & 0 & 0 & 0 & 0 & -\frac{1}{2H_a} \\ 0 & -\frac{1}{T_t} & \frac{1}{T_t} & 0 & 0 & 0 & 0 & 0 & 0 & 0 \\ -\frac{1}{R_a T_g} & 0 & -\frac{1}{T_g} & 0 & 0 & 0 & 0 & 0 & 0 & 0 \\ 0 & 0 & 0 & -\frac{1}{T_{WT}} & 0 & 0 & 0 & 0 & 0 & 0 \\ 0 & 0 & 0 & 0 & -\frac{D_b}{2H_b} & \frac{1}{2H_b} & 0 & 0 & \frac{1}{2H_b} & \frac{1}{2H_b} \\ 0 & 0 & 0 & 0 & \frac{2T_R}{R_b T_1 T_2} & -\frac{2}{T_w} & \frac{2T_2+2T_w}{T_2 T_w} & \frac{2T_R-2T_1}{T_1 T_2} & 0 & 0 \\ 0 & 0 & 0 & 0 & -\frac{T_R}{R_b T_1 T_2} & 0 & -\frac{1}{T_2} & \frac{T_1-T_R}{T_1 T_2} & 0 & 0 \\ 0 & 0 & 0 & 0 & -\frac{1}{R_b T_1} & 0 & 0 & -\frac{1}{T_1} & 0 & 0 \\ 0 & 0 & 0 & 0 & 0 & 0 & 0 & 0 & -\frac{1}{T_{PV}} & 0 \\ 2\pi T_{tie,eq} & 0 & 0 & 0 & -2\pi T_{tie,eq} & 0 & 0 & 0 & 0 & 0 \end{bmatrix} \quad (12)$$

$$B_1 = \begin{bmatrix} -\frac{1}{2H_a} & 0 & 0 & 0 \\ 0 & 0 & 0 & 0 \\ 0 & 0 & 0 & 0 \\ 0 & \frac{K_{WT}}{T_{WT}} & 0 & 0 \\ 0 & 0 & -\frac{1}{2H_b} & 0 \\ 0 & 0 & 0 & 0 \\ 0 & 0 & 0 & 0 \\ 0 & 0 & 0 & 0 \\ 0 & 0 & 0 & \frac{K_{PV}}{T_{PV}} \\ 0 & 0 & 0 & 0 \end{bmatrix}, \text{ and } \quad B_2 = \begin{bmatrix} 0 & -\frac{1}{2H_a} & 0 & 0 \\ 0 & 0 & 0 & 0 \\ -\frac{1}{T_g} & 0 & 0 & 0 \\ 0 & 0 & 0 & 0 \\ 0 & 0 & 0 & -\frac{1}{2H_b} \\ 0 & 0 & \frac{2T_R}{T_1 T_2} & 0 \\ 0 & 0 & -\frac{T_R}{T_1 T_2} & 0 \\ 0 & 0 & -\frac{1}{T_1} & 0 \\ 0 & 0 & 0 & 0 \\ 0 & 0 & 0 & 0 \end{bmatrix} \quad (13)$$

$$C = \begin{bmatrix} 1 & 0 & 0 & 0 & 0 & 0 & 0 & 0 & 0 & 0 \\ B_a & 0 & 0 & 0 & 0 & 0 & 0 & 0 & 0 & 1 \\ 0 & 0 & 0 & 0 & 1 & 0 & 0 & 0 & 0 & 0 \\ 0 & 0 & 0 & 0 & B_b & 0 & 0 & 0 & 0 & -1 \end{bmatrix} \quad (14)$$

Table 1. Numerical values for the studied power grid models ($x \in \{a, b\}$), [65].

Parameters	Symbols	Value	
		Area a	**Area b**
Capacity (rated)	P_{rx} (MW)	1200	1200
Drooping constants	R_x (Hz/MW)	2.4	2.4
Frequency bias	B_x (MW/Hz)	0.4249	0.4249
Valve gates limiting minimum	V_{vlx} (p.u.MW)	−0.5	−0.5
Valve gates limiting maximum	V_{vux} (p.u.MW)	0.5	0.5
Time constant (thermal governors)	T_g (s)	0.08	-
Time constant (thermal turbines)	T_t (s)	0.3	-
Time constant (hydraulic governors)	T_1 (s)	-	41.6
Time constants (hydraulic governor)	T_2 (s)	-	0.513
Reset time (hydraulic governors)	T_R (s)	-	5
Starting time of water (hydraulic turbines)	T_w (s)	-	1
Inertia constant	H_x (p.u.s)	0.0833	0.0833
Damping coefficient	D_x (p.u./Hz)	0.00833	0.00833
Time constants (PV generations)	T_{PV} (s)	-	1.3
Gains (PV generations)	K_{PV} (s)	-	1
time constants (wind generations)	T_{WT} (s)	1.5	-
Gains (wind generations)	K_{WT} (s)	1	-
EV Models			
Penetration level	-	5–10%	5–10%
Voltages (nominal values)	V_{nom} (V)	364.8	364.8
Batteries capacities	C_{nom} (Ah)	66.2	66.2
Series resistances	R_s (ohms)	0.074	0.074
Transient resistances	R_t (ohms)	0.047	0.047
Transient capacitances	C_t (farad)	703.6	703.6
Constant values	RT/F	0.02612	0.02612
Battery's SOC (minimum SOC)	%	10	10
Battery's SOC (maximum SOC)	%	95	95
Battery's energy capacity	C_{batt} (kWh)	24.15	24.15

3. The Proposed TFOIDFF Controller

3.1. The FO Calculus Theory

Related to FO calculus representation, several approaches have been presented in the literature. The commonly employed definitions for FO calculus are the Grunwald–Letnikov approach, the Riemann–Liouville approach, and the Caputo approach [66]. The Grunwald–Letnikov approach defines α_{th} FO derivative for function f within a to t limits as follows [67]:

$$D^{\alpha}\big|_a^t = \lim_{h \to 0} \frac{1}{h^{\alpha}} \sum_{r=0}^{\frac{t-a}{h}} (-1)^r \binom{n}{r} f(t - rh) \tag{15}$$

where, h denotes the step time, and operator $[\cdot]$ takes the integer parts only from the previous argument. Whereas, n variable should satisfy the following condition ($n - 1 < \alpha < n$). The coefficients of binomial can be defined as follows [67]:

$$\binom{n}{r} = \frac{\Gamma(n+1)}{\Gamma(r+1)\Gamma(n-r+1)'} \tag{16}$$

where, the gamma function is defined using the well-known representation as following [66]:

$$\Gamma(n+1) = \int_0^{\infty} t^{x-1} e^{-t} \, dt \tag{17}$$

Liouville and Riemann have proposed a definition for the FO derivative, which avoids the use of sum and limit. Instead, it uses the IO derivative, and integral representations, as follows [68]:

$$D^{\alpha}|_a^t = \frac{1}{\Gamma(n-\alpha)} \left(\frac{d}{dt}\right)^n \int_a^t \frac{f(\tau)}{(t-\tau)^{\alpha-n+1}} \, d\tau \tag{18}$$

Another method for defining FO derivative was presented by Caputo, which can be expressed as follows [67]:

$$D^{\alpha}|_a^t = \frac{1}{\Gamma(n-\alpha)} \int_a^t \frac{f^{(n)}(\tau)}{(t-\tau)^{\alpha-n+1}} \, d\tau \tag{19}$$

The general FO operators $D^{\alpha}|_a^t$, can represent several forms as follows:

$$D^{\alpha}|_a^t = \begin{cases} \alpha > 0 \ \rightarrow \ \frac{d^{\alpha}}{dt^{\alpha}} & \text{FO derivative} \\ \alpha < 0 \ \rightarrow \ \int_{t_0}^{t_f} dt^{\alpha} & \text{FO integral} \\ \alpha = 0 \ \rightarrow \ 1 \end{cases} \tag{20}$$

For implementing FO control, the Oustaloup recursive approximation (ORA) of FO derivative was reported to be suitable for real-time digital implementation [66]. The ORA has become more familiar regarding the optimal tuning processes of FO controllers. Due to its widespread presence in the literature, the ORA is employed in this paper for modeling FO integrals and derivatives. The approximate mathematical representation of the αth FO derivative (s^{α}) is expressed as follows [66]:

$$s^{\alpha} \approx \omega_h^{\alpha} \prod_{k=-N}^{N} \frac{s + \omega_k^z}{s + \omega_k^p} \tag{21}$$

where, ω_k^p and ω_k^z denote the poles, and zeros for the sequence ω_h. They can be calculated as follows:

$$\omega_k^z = \omega_b \left(\frac{\omega_h}{\omega_b}\right)^{\frac{k+N+\frac{1-\alpha}{2}}{2N+1}} \tag{22}$$

$$\omega_k^p = \omega_b \left(\frac{\omega_h}{\omega_b}\right)^{\frac{k+N+\frac{1+\alpha}{2}}{2N+1}} \tag{23}$$

$$\omega_h^{\alpha} = \left(\frac{\omega_h}{\omega_b}\right)^{\frac{-\alpha}{2}} \prod_{k=-N}^{N} \frac{\omega_k^p}{\omega_k^z} \tag{24}$$

where, the approximate FO operator's function has $(2N+1)$ poles/zeros number. Thus, the number N defines the ORA filter order (order equals $(2N+1)$). In this paper, the ORA is used with $(M = 5)$ in the frequency range ($\omega \in [\omega_b, \omega_h]$), where it is selected to be between $[10^{-3}, 10^3]$ rad/s.

3.2. Existing IO and FO LFC Methods

The control family of PID is well-known for linear control, and has been widely employed for several industrial applications, and in particular for LFC in different forms. Each gain performs a specific task to decrease the rise time, and to reduce steady-state errors in the time-domain response of the controlled system [69]. The derivative gains are responsible for increasing system stability and for reducing overshoot/undershoot values. However, they amplify high-frequency noise in the system. The integral gains are responsible for eliminating steady-state errors; however, they worsen the transient

response of the system. The transfer functions of widely employed IO LFCs are represented as follows:

$$C_{PI}(s) = \frac{Y(s)}{E(s)} = K_p + \frac{K_i}{s}$$

$$C_{PID}(s) = \frac{Y(s)}{E(s)} = K_p + \frac{K_i}{s} + K_d\, s \tag{25}$$

$$C_{PIDF}(s) = \frac{Y(s)}{E(s)} = K_p + \frac{K_i}{s} + K_d\, s\, \frac{N_f}{s + N_f}$$

From another standpoint, FO controllers have been reported to improve overall system performance compared with IO-based counterparts [70]. The transfer functions of widely employed FO LFCs are represented as follows:

$$C_{FOPI}(s) = \frac{Y(s)}{E(s)} = K_p + \frac{K_i}{s^\lambda}$$

$$C_{FOPID}(s) = \frac{Y(s)}{E(s)} = K_p + \frac{K_i}{s^\lambda} + K_d\, s^\mu$$

$$C_{FOPIDF}(s) = \frac{Y(s)}{E(s)} = K_p + \frac{K_i}{s^\lambda} + K_d\, s^\mu\, \frac{N_f}{s + N_f} \tag{26}$$

$$C_{TID}(s) = \frac{Y(s)}{E(s)} = K_t\, s^{-\left(\frac{1}{n}\right)} + \frac{K_i}{s} + K_d\, s$$

$$C_{TIDF}(s) = \frac{Y(s)}{E(s)} = K_t\, s^{-\left(\frac{1}{n}\right)} + \frac{K_i}{s} + K_d\, s\, \frac{N_f}{s + N_f}$$

It can be seen from (25), and (26) that FO controllers have more tunable parameters than their IO counterparts. For instance, the FOPID ($PI^\lambda D^\mu$ has five tunable parameters compared to three parameters in the PID controller. Figure 4 shows the widely employed IO- and FO-based LFCs in the literature.

3.3. The Proposed TFOIDFF Controller

Figure 5 shows a schematic diagram of the proposed TFOIDFF controller. It includes the tilt branch from the TID control, the FO ID from the FOPID control, and the FF with the derivative branch. Therefore, the resulting proposed TFOIDFF controller can be expressed as follows:

$$C(s) = \frac{Y(s)}{E(s)} = K_t\, s^{-\left(\frac{1}{n}\right)} + \frac{K_i}{s^\lambda} + K_d\, s^\mu\, \frac{N_f}{s^{\lambda_f} + N_f} \tag{27}$$

where, K_t, K_i, K_d stand for tilt, integral, and derivative gains. Whereas, λ, λ_f and μ are the FO operators of integral, fractional filter, and derivative terms. In addition, n is the tilt FO power, and N_f is the FF coefficient. The main characteristics of the new proposed TFOIDFF controller are as follows:

1. The use of tilt FO branch instead of IO proportional term adds more flexibility to the design of the proposed TFOIDFF controller. The tilt term can also improve the disturbance-rejection ability and enhance controller robustness against parametric uncertainty.
2. The use of FO integrator and derivative FO terms combines the benefits of the FOPID control with the tilt term. The FO ID terms provide more opportunities for flexible design compared with IO-based PID controller. Merging the two controllers adds more flexibility and freedom to the new proposed TFOIDFF controller.
3. The use of the fractional filter adds a low-pass filtering property in addition to the FO operator. The use of FF helps at solving the realizability problem of the derivative term. Although the derivative term improves the stability and reduced overshoot response, it amplifies the high-frequency noise. Thus, a filtering stage is needed with the derivative term. Furthermore, the FF helps in mitigating the derivative's kick

effects, which result from instantaneous changes in the input signal of the controller (ACE signals). These effects are eliminated though the employed FF component.
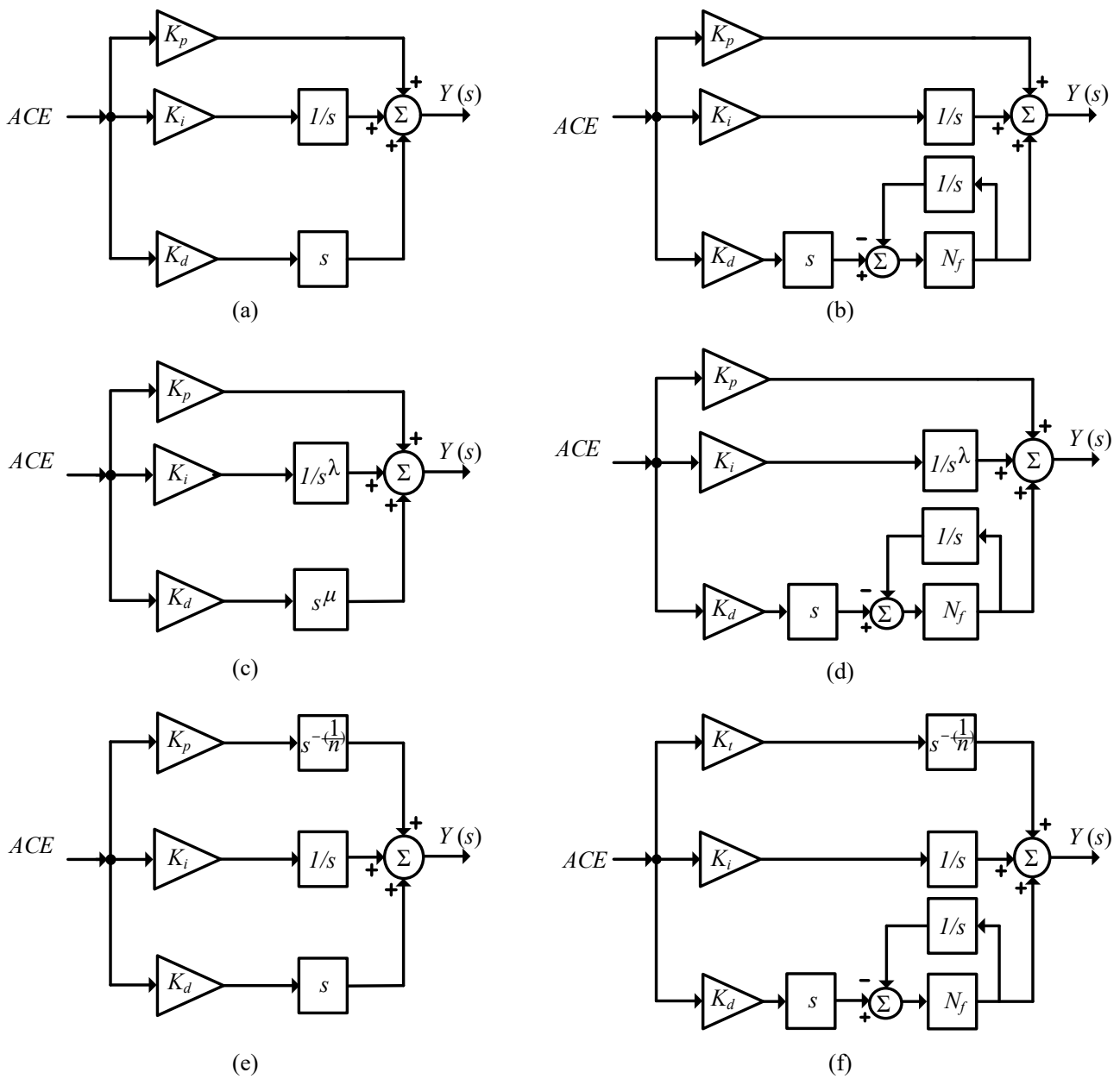

Figure 4. Widely employed IO- and FO-based LFCs from the literature. (**a**) PID controller; (**b**) PIDF controller; (**c**) FOPID controller; (**d**) FOPIDF controller; (**e**) TID controller; (**f**) TIDF controller.
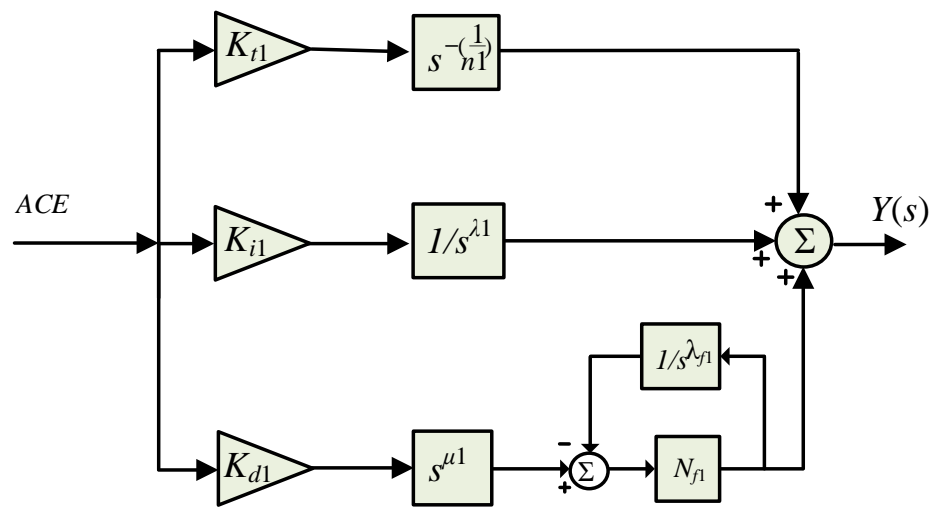
Figure 5. The proposed TFOIDFF controller.

4. The Proposed AHA-Based Parameter Optimization

4.1. Optimization Process of the Proposed TFOIDFF Controller

For proper functionality of the proposed TFOIDFF controller in the two-area power grid, optimized parameter values are needed. Owing to recent advancements in meta-heuristic optimization methods, proper tuning of control parameters can be simultaneously achieved for both of the interconnected areas. Therefore, global optimum values are obtained for the whole system. This process leads to better transient response and enhanced steady-state performance. The proposed TFOIDFF controller is installed in each area to produce the centralized control functionality of LFC and EVs in each area. The proposed TFOIDFF contains eight parameters, which are adjusted for the desired objective of the system. Among the existing objective function representations, the Integral-squared-error (ISE) demonstrates superior performance in the literature, and it is selected for implementing the proposed controller in this paper. The ISE is generally expressed as follows:

$$ISE = \int \sum_{i=1}^{m}(e_i^2) \, \mathrm{d}t \tag{28}$$

In the current optimization problem, the proposed TFOIDFF controller has to set frequency deviations at their minimum values in each studied area (Δf_a and Δf_b), and eliminates tie-line power fluctuations among areas (($\Delta P_{tie,ab}$)). The three controlled variables can be included in the ISE function of the proposed optimization process as follows:

$$ISE = \int_{0}^{t_s} ((\Delta f_a)^2 + (\Delta f_b)^2 + (\Delta P_{tie})^2) \, \mathrm{d}t \tag{29}$$

Thus, 8 tunable controller parameters exist in each area, forming a total of 16 tunable controller parameters in the proposed optimization process. Figure 6 shows the optimization process of controller parameters. The tunable controller parameters are constrained by their lower/upper limits as follows:

$$K_t^{min} \leq K_{t1}, K_{t2} \leq K_t^{max}$$
$$K_i^{min} \leq K_{i1}, K_{i2} \leq K_i^{max}$$
$$K_d^{min} \leq K_{d1}, K_{d2} \leq K_d^{max}$$
$$n^{min} \leq n_1, n_2 \leq n^{max}$$
$$\lambda^{min} \leq \lambda_1, \lambda_2 \leq \lambda^{max} \qquad (30)$$
$$\mu^{min} \leq \mu_1, \mu_2 \leq \mu^{max}$$
$$N_f^{min} \leq N_{f1}, N_{f2} \leq N_f^{max}$$
$$\lambda_f^{min} \leq \lambda_{f1}, \lambda_{f2} \leq \lambda_f^{max}$$

where, $(f)^{min}$ and $(f)^{max}$ stand for lower limits and upper limits of tunable controller parameter values, respectively. Whereas, $(K_t^{min}, K_i^{min}, K_d^{min})$ are placed at zero, and $(K_p^{max}, K_t^{max}, K_i^{max}, K_d^{max})$ are set at 2 within the proposed process. The value of (n^{min}) is placed at 2, whereas (n^{max}) is placed at 10. The values of μ^{min}, λ^{min} and λ_f^{min}, are placed at 0, whereas μ^{max}, λ^{max} and λ_f^{max} are placed at 1. The values of N_c $(N_c^{min}$, and $N_c^{max})$ are placed at 5, and 400, respectively.
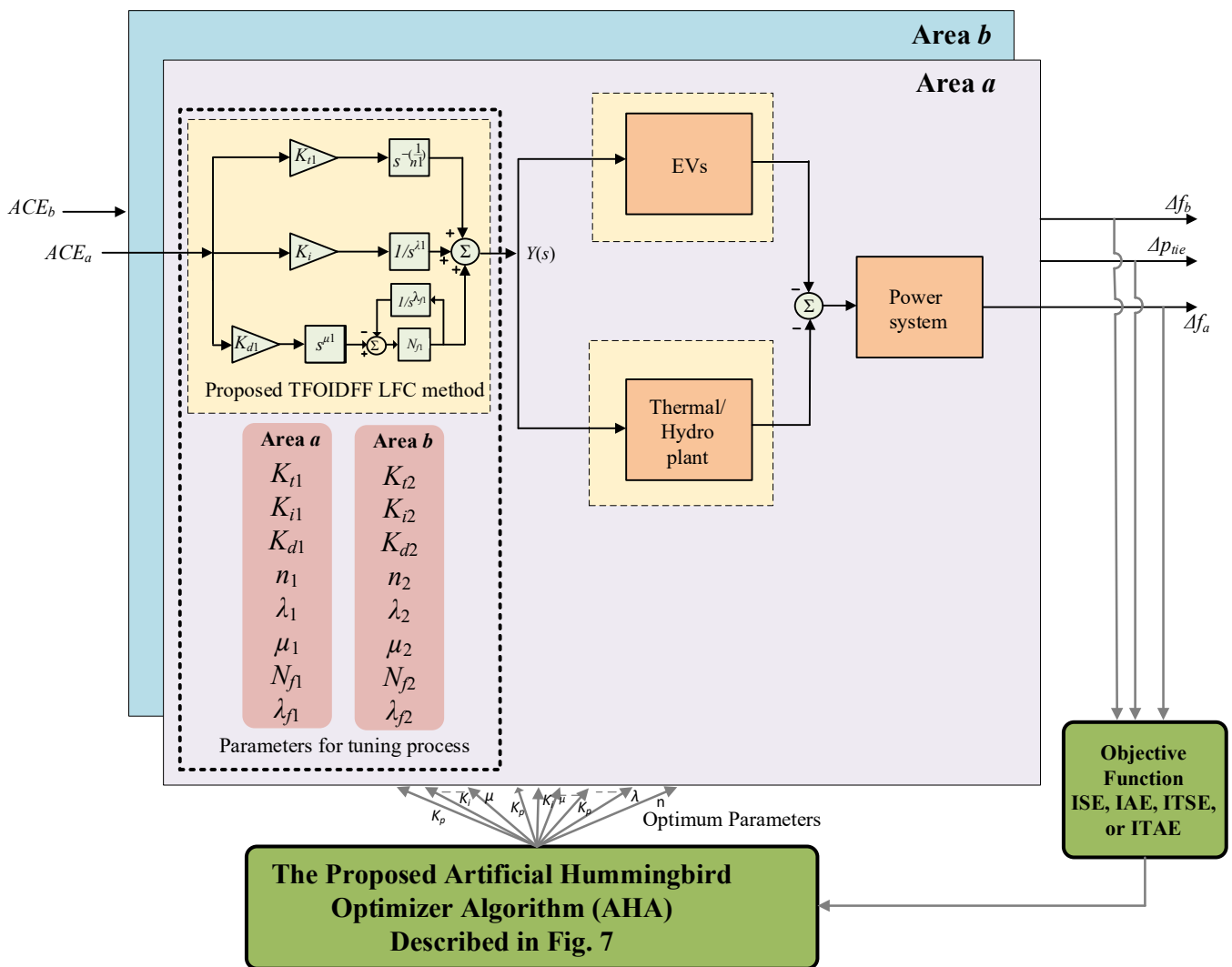

Figure 6. The proposed AHA-based optimized TFOIDFF controller.

4.2. The Artificial Hummingbird Optimizer

The artificial hummingbird optimizer algorithm (AHA) was recently introduced in [57]. It represents a bio-inspired optimizer approach, and is inspired by the special flight skills of hummingbirds during intelligent foraging and hunting for prey. The selection of food sources represents the initial step of AHA implementation, in which, proper food sources are selected by hummingbirds based on nectar quality, content of individual flowers, nectar refilling rate, and their last visit time regarding flowers.

In the AHA optimizer, solution vector is represented by food sources, while the fitness value is represented by nectar refilling rate [59]. Better fitness values can be obtained at higher nectar refilling rates. Each hummingbird is assigned to a certain source of food, which signifies that the food source and the hummingbird are at the same position. It then memorizes the food sources' positions, and nectar refilling rates. In addition, it shares information with others in the population. Furthermore, it minds the period of last visit of food sources. Thus, a schedule named-visit table is used to record the assigned visit activity level for each hummingbird. Priority is given to food sources with higher visitation levels from the hummingbirds [58].

For obtaining more nectar, the hummingbirds tend to visit food sources with the highest nectar refilling rate among others that have same high visitation levels [71]. Thus, hummingbirds are able to evaluate their own targeted food sources through using the visits table, which is updated within the iterative processes. Three different behaviors of foraging are performed in the AHA optimizer by hummingbirds, namely the guided, territorial, and migrating behaviors. For constructing the model, which mimics the behavior of hummingbirds, initial populations with n hummingbirds are generated randomly based on search-space limits as follows [57]:

$$x_i = Lw + rand \times (Up - Lw) \ , i = 1, 2, ..., n \tag{31}$$

where, x_i stands for the ith position of food source, Lw and Up denotes the lower, and the upper problem search-space bounds, and $rand$ represents a random number between [0, 1]. The visit table of food sources is initialized as follows [57]:

$$VT_{i,j} = \begin{cases} 0, & i \neq j \\ null, & i = j \end{cases} \quad i = 1, 2, ..., n \quad \text{and} \quad j = 1, 2, ..., n \tag{32}$$

4.2.1. The Guided Foraging

The hummingbirds tend to visit food sources with the highest volumes of nectar. Therefore, the targeted source requires high nectar refilling rates, as a long consumption time by the hummingbirds is undesirable. Therefore, hummingbirds determine food sources with the highest levels of visitation and select nectar with the highest refilling rates as their targets. Afterwards, hummingbirds devour the food by flying to this position. A total of three hummingbird flight skills, including the omni-directional, diagonal, and axial skills are employed to model the AHA optimizer. The selection and control of flight skills are achieved through a direction-switching vector, which decides the conducted directions (whether only one, or more than one) in the search-space with dimensions. During axial flight, hummingbirds fly along the coordinate axis. Whereas, during diagonal flight, movements are made from one corner directed to the opposite corner. Axial flight is expressed as follows [57]:

$$D_i = \begin{cases} 1, & i = randi([1, d]) \\ 0, & \text{Otherwise} \end{cases} \quad i = 1, 2, ..., d \tag{33}$$

whereas, diagonal flights are expressed as follows [71]:

$$D_i = \begin{cases} 1, & i = P(j), j \in [1, k], P = randperm(k), k \in [2, [r_1.(d-2)] + 1] \\ 0, & \text{Otherwise} \end{cases} \quad i = 1, 2, ..., d \tag{34}$$

Moreover, omni-directional flights are represented as follows [57]:

$$D_i = 1, \quad i = 1, 2, ..., d \tag{35}$$

where, $randi([1, d])$ stands for random number vector generated from 1 to d, $randperm(k)$ generates the random alteration between 1 and k, and r_1 stand for a random number between $[0, 1]$. Hummingbirds visit targeted food sources using these flights capabilities. Thus, food sources are updated using the old ones, and other selected targeted sources. The guided foraging is expressed as follows [71]:

$$v_i^{(t+1)} = x_{i,t}^{(t)} + \alpha D(x_i^{(t)} - x_{i,t}^{(t)}), \quad \alpha N(0, 1) \tag{36}$$

where $x_i^{(t)}$ stands for food source with number i at the iteration t, $x_{i,t}^{(t)}$ denotes the ith targeted food source during iteration t, and α stands for guided factor, which follows normal distributions. The food source position is updated as follows [57]:

$$x_i^{(t+1)} = \begin{cases} x_i^{(t)}, & f(x_i^{(t)}) \le f(v_i^{(t+1)}) \\ v_i^{(t+1)}, & f(x_i^{(t)}) > f(v_i^{(t+1)}) \end{cases} \tag{37}$$

where, f stands for fitness value.

4.2.2. The Territorial Foraging

Hummingbirds search for new sources of food after consuming flower nectar via movement to their neighbor regions. The new food sources might be better than current ones. The followed local search in territorial foraging is expressed as follows [57]:

$$v_i^{(t+1)} = x_{i,t}^{(t)} + bDx_i^{(t)}, \quad bN(0, 1) \tag{38}$$

where b stands for territorial factor, which follows a normal distribution function.

4.2.3. The Migration Foraging

The hummingbirds typically migrate to food sources in areas too far away for feeding themselves when food shortages occur in their frequently visited area. In the AHA optimizer, migration factor can be specified. In cases where the iteration number exceeds the migration factor's preset value, hummingbirds at food sources with the worst refilling rate of nectar move to a new source. This, in turn, represents the randomly produced food source within the entire searching space. Then, this hummingbird abandons the old food source and remains at the new food source. Afterwards, the visitation schedule is updated. The migration of hummingbirds from a food source having the worst refilling rate of nectar to a new source can be expressed as follows [57]:

$$x_{worst}^{(t+1)} = Lw + rand \times (Up - Lw) \tag{39}$$

where, $x_{worst}^{(t+1)}$ stands for the worst refilling rate of nectar sources at the iteration $(t + 1)$. The AHA algorithm flowchart with main steps for optimizing the proposed TFOIDFF controller is shown in Figure 7.
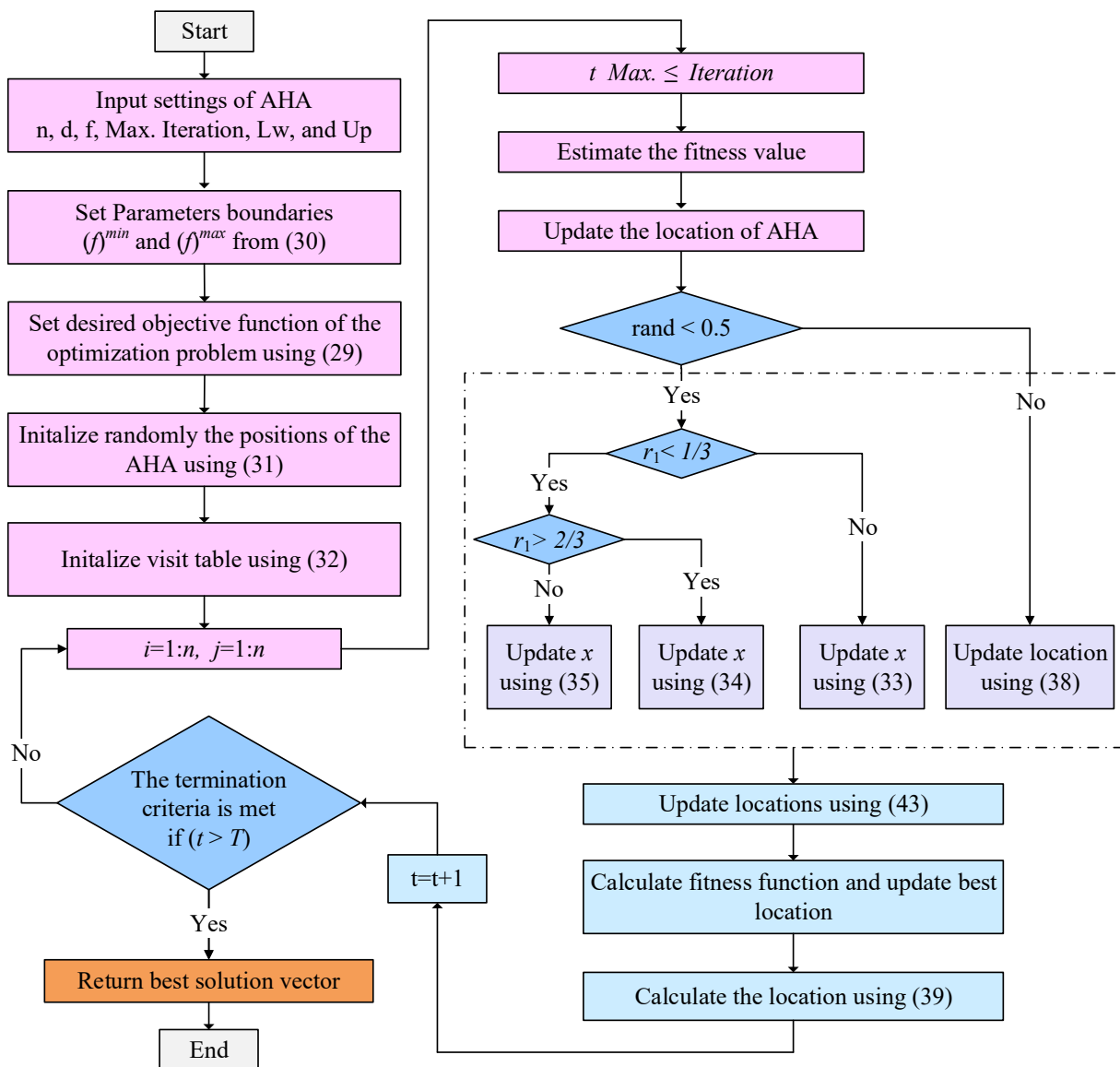
Figure 7. The AHA algorithm flowchart with main steps for optimizing the proposed TFOIDFF controller.

5. Results and Discussions

This section discusses the validation and efficacy of the novel TFOIDFF controller implementation, coordinated with EVs for improving the LFC of interconnected power grid systems, shown in Figure 3. A newly proposed AHA optimizer has been applied for tuning the different control parameters of TFOIDFF and other controllers in the literature for fair comparison. The AHA technique is developed using the m-file code of MATLAB program and was interfaced with the Simulink system of the studied interconnected power grid to accomplish the LFC objective function. The Simulink multi-area power grid system with the AHA optimization technique is implemented utilizing a personal computer with an Intel Core i7 2.9 GHz CPU, 64-bit version. Table 2 shows the obtained AHA-based optimized controller parameters for the selected case study. To assess the robustness of the proposed TFOIDFF controller, it is compared with conventional and advanced control techniques, such as PIDF, TIDF, FOPIDF, and FOTIDF using the same coordination with the EV system based on the AHA technique. In addition, the comparisons are held under the same operation conditions of load demand and RES perturbations of the studied multi-area power grid system, which includes a decentralized TFOIDFF for the LFC and EV system to

preserve microgrid dynamic security. The results are investigated for the studied multi-area power grid system under different case studies over the following scenarios.

Table 2. The AHA-based obtained optimal controller parameters.

Control	Area	Coefficients								
		K_t	K_p	K_i	K_d	λ	μ	n	N_f	λ_f
PIDF	Area *a*	—	1.3053	1.7534	0.8453	—	—	—	214	—
	Area *b*	—	1.3053	1.7534	0.8453	—	—	—	214	—
TIDF	Area *a*	1.9062	—	1.8547	1.8637	—	—	2.94	284	—
	Area *b*	1.8021	—	1.9562	1.8454	—	—	3.2	302	—
FOPIDF	Area *a*	—	2.1342	2.0145	1.4823	0.921	0.825	—	322	—
	Area *b*	—	2.6079	1.3671	1.9885	0.741	0.823	—	254	—
FOTIDF	Area *a*	1.8184	—	1.5672	0.9969	0.468	0.758	4.95	297	—
	Area *b*	1.9885	—	1.1894	1.9497	0.566	0.547	4.23	239	—
TFOIDFF	Area *a*	1.9851	—	1.6332	1.7719	0.592	0.911	4.07	366	0.88
	Area *b*	1.5311	—	1.1018	2.8191	0.697	0.762	3.2	369	0.58

5.1. Scenario 1

A 10% step load perturbation (SLP) at zero second is applied in area *a* to validate the effectiveness of the proposed TFOIDFF controller coordinated with EV in the LFC loop over the other conventional and advanced control techniques, which are conferred in the literature as means of assessment based on the new AHA technique. Moreover, the AHA is verified during this scenario against other algorithms in the literature as depicted in Figures 8–11 for ISE, IAE, ITSE, and ITAE objective functions, respectively. It can be seen that for all the objective functions, the proposed AHA optimization process bears faster and better conversion characteristics than the studied PSO, ABC, BOA, and AEO optimizers.
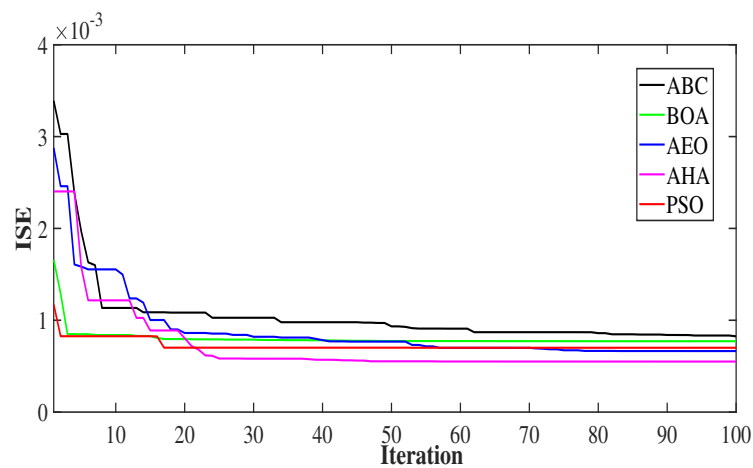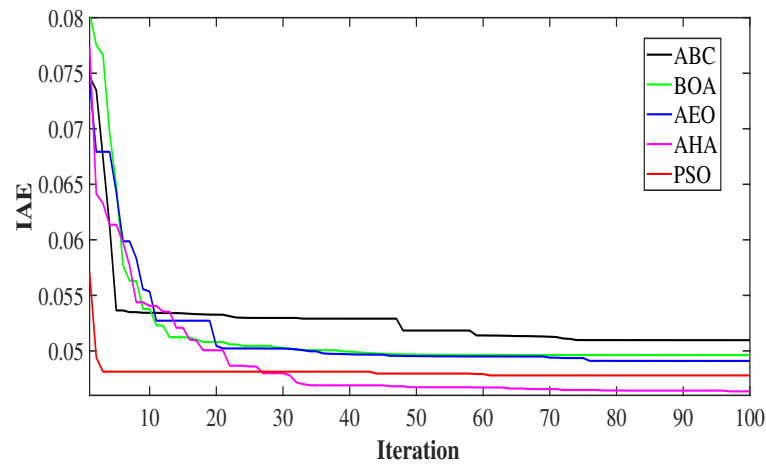

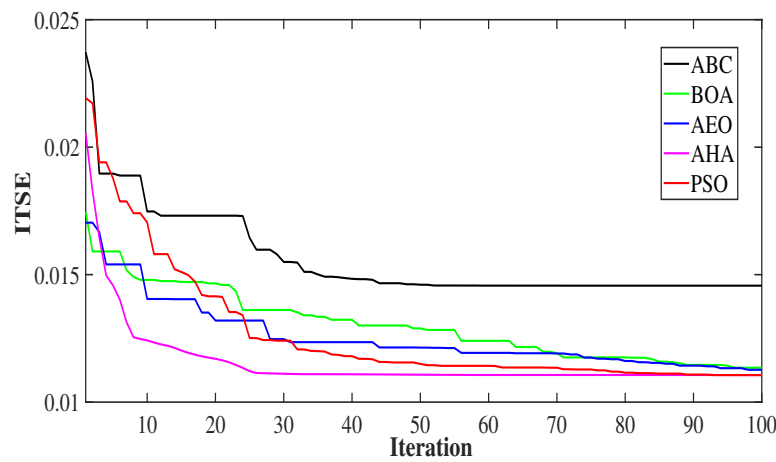**Figure 8.** The ISE comparison.

Figure 9. The IAE comparison.

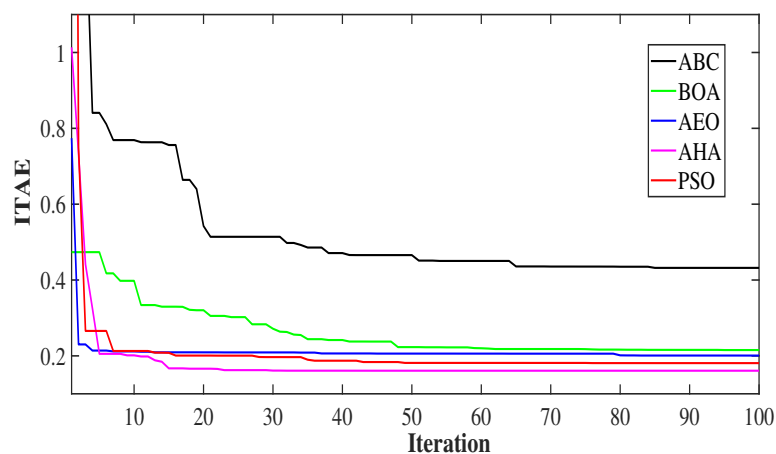**Figure 10.** The ITSE comparison.

Figure 11. The ITAE comparison.

The frequency and tie-line power responses (Δf_1, Δf_2, and ΔP_{tie}), of the studied multi-area power grid system of both area *a* and area *b* are visualized in Figure 12, respectively. This figure includes the comparison of the proposed control with all four controllers to obtain the best coordination with EV system based on the proposed AHA optimization method. It can be observed that the proposed TFOIDFF controller provides better system stability and enhanced damping characteristics with fewer oscillations than other

controllers. Whereas, it can produce 0.002 Hz and 0.001 Hz frequency deviations in area *a* and area *b*, respectively, with 0.0005 p.u deviation in tie-line power comparison with another family member FOTIDF controller, which has deviations of 0.003 Hz, 0.0023 Hz and 0.0006 p.u for Δf_1, Δf_2, and ΔP_{tie}, respectively.

(**a**)

(**b**)

(**c**)
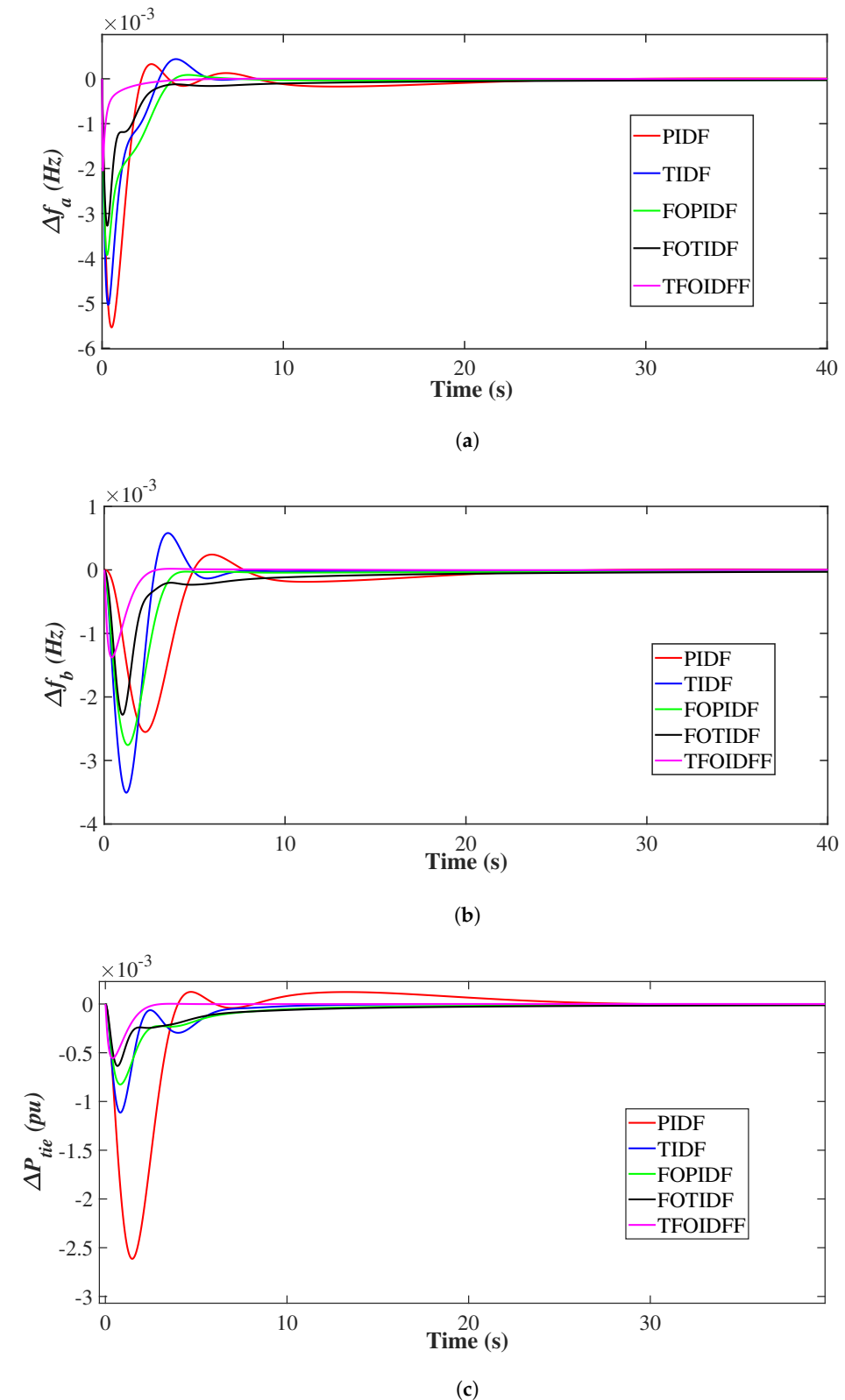
Figure 12. System responses in Scenario 1. (**a**) Δf_a; (**b**) Δf_b; (**c**) ΔP_{tie}.

Meanwhile, the other fractional-order controller FOPIDF provides 0.004 Hz in area *a* and 0.0027 Hz in area *b* with tie-line deviation at 0.0008 p.u. Furthermore, the TIDF and PIDF give the worst deviations in this case with 0.005 Hz and 0.0055 Hz in area *a*, respectively. A complete comparison analysis for the suggested controllers is recorded in Table 3 for different criteria such as, settling time (Ts), maximum overshoot (MO), and maximum undershoot (MU). On the other hand, Figure 13 shows that the proposed AHA technique has confirmed its robustness not only against different controllers but also compared to conventional PSO and AEO optimization methods. The AHA design can suppress frequency fluctuations in both areas to very low values in terms of MO and MU as shown in Figure 13a,b and with minimum Ts in this case. In addition, the proposed AHA-based design provides the best performance regarding mitigation of tie-line power deviations compared to other techniques as depicted in Figure 13c. Therefore, the proposed AHA design provides superior robustness and effectiveness performance with the proposed TFOIDFF controller over other comparative methods.

Table 3. Performance comparisons at the tested scenarios.

No.	Controller	Δf_a			Δf_b			ΔP_{tie}		
		PO	PU	ST	PO	PU	ST	PO	PU	ST
	PIDF	0.0006	0.0055	28	0.0002	0.0028	26	0.0001	0.0026	28
	TIDF	0.0008	0.0051	12	0.0005	0.0035	16	0.00006	0.0011	17
No.1	FOPIDF	0.0002	0.0039	15	—	0.0027	18	0.0002	0.0008	15
	FOTIDF	0.0012	0.0033	23	0.0002	0.0023	32	0.0002	0.0006	28
	TFOIDFF	—	0.0020	6	—	0.0013	11	—	0.0005	5
	PIDF	0.0032	0.0082	30	0.0045	0.0073	19	0.0002	0.0024	>40
	TIDF	0.0017	0.0065	19	0.0025	0.0061	15	0.0003	0.0014	18
No.2	FOPIDF	0.0007	0.0055	23	0.0009	0.0048	22	0.00001	0.0011	25
	FOTIDF	0.0001	0.0048	18	0.0002	0.0042	26	0.0001	0.0008	>40
	TFOIDFF	—	0.0035	9	—	0.0036	10	—	0.0004	9
	PIDF	0.0011	0.0091	36	0.0001	0.0146	21	0.0064	0.0017	26
No.3	TIDF	0.0004	0.0078	38	0.0005	0.0112	34	0.0032	0.0002	33
	FOPIDF	—	0.0074	22	0.0018	0.0099	18	0.0030	—	17
(40 s)	FOTIDF	—	0.0068	17	0.00002	0.0103	12	0.0027	—	13
	TFOIDFF	—	0.0026	8	—	0.0052	9	0.0005	—	8
	PIDF	0.0878	0.0078	13	0.0537	0.0133	17	0.0241	0.0015	31
No.4	TIDF	0.0698	0.0028	11	0.0421	0.0025	14	0.0232	0.0053	22
	FOPIDF	0.0581	0.0148	21	0.0224	0.0131	19	0.0185	0.0015	18
(85 s)	FOTIDF	0.0573	0.0055	23	0.0202	0.0026	23	0.0143	0.0026	27
	TFOIDFF	0.0169	—	7	0.0117	—	12	0.0047	—	11
	PIDF	0.1105	0.0110	FU	0.0691	0.0181	FU	0.0248	0.0024	FU
No.5	TIDF	0.0885	0.0211	FU	0.0552	0.0424	FU	0.0232	0.0059	FU
	FOPIDF	0.0751	0.0082	23	0.0550	0.0072	24	0.0191	0.0037	22
(70 s)	FOTIDF	0.0545	0.0101	19	0.0195	0.0126	20	0.0163	0.0039	19
	TFOIDFF	0.0351	—	11	0.0112	—	10	0.0064	—	13
	PIDF	0.1497	0.0088	FU	0.1841	0.0317	FU	0.0102	0.0305	FU
No.6	TIDF	0.1224	0.0166	FU	0.1622	0.0149	FU	0.0251	0.0021	FU
	FOPIDF	0.1039	0.0271	FU	0.1011	0.0087	FU	0.0163	0.0015	FU
(40 s)	FOTIDF	0.0691	0.0098	FU	0.0934	0.0163	22	0.0099	0.0066	FU
	TFOIDFF	0.0313	—	11	0.0029	—	12	0.0046	0.0005	15

FU represents Fluctuated response conditions.

(**a**)

(**b**)

(**c**)
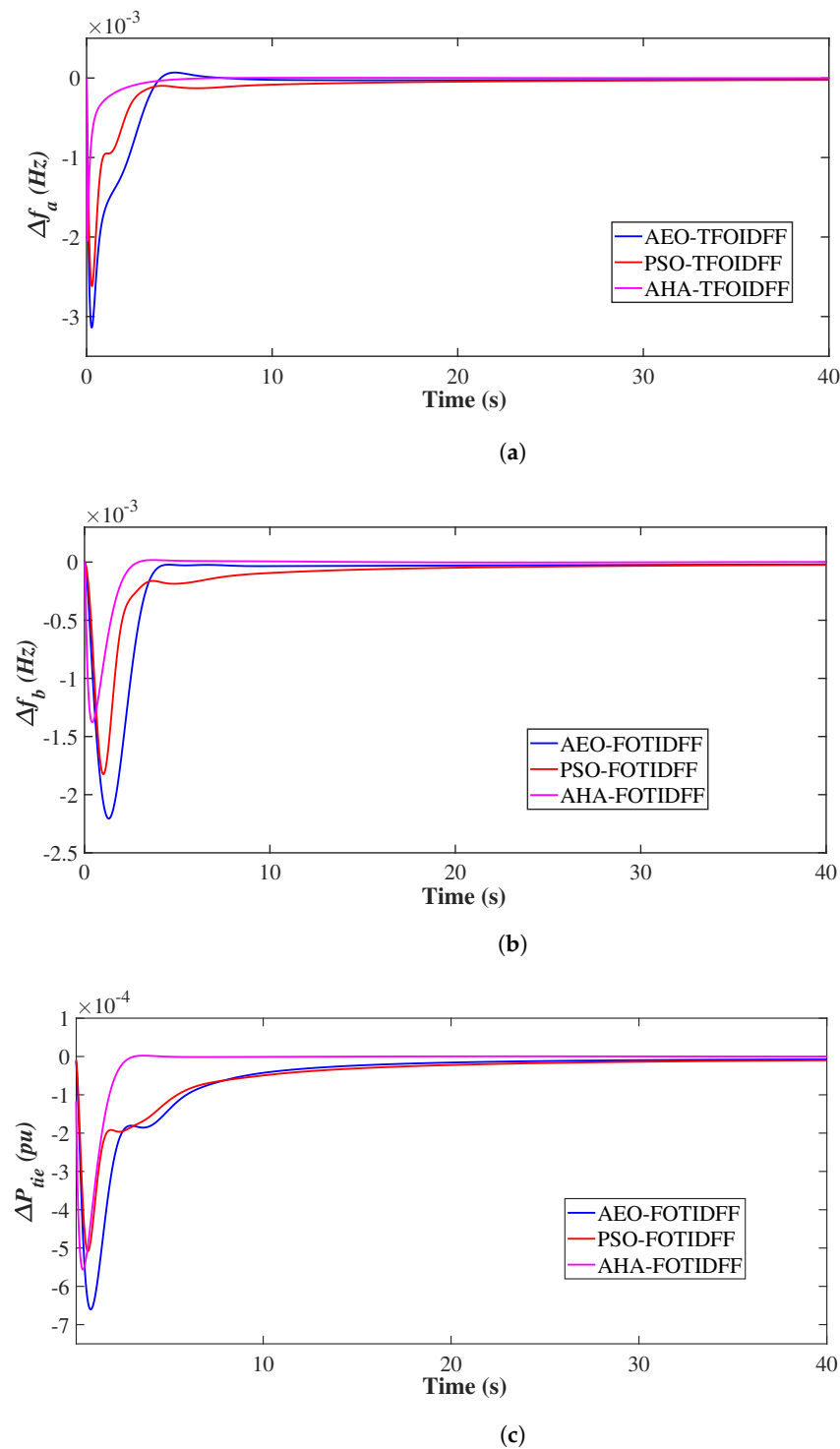
Figure 13. System responses in Scenario 1 for different algorithms. (**a**) Δf_a; (**b**) Δf_b; (**c**) ΔP_{tie}.
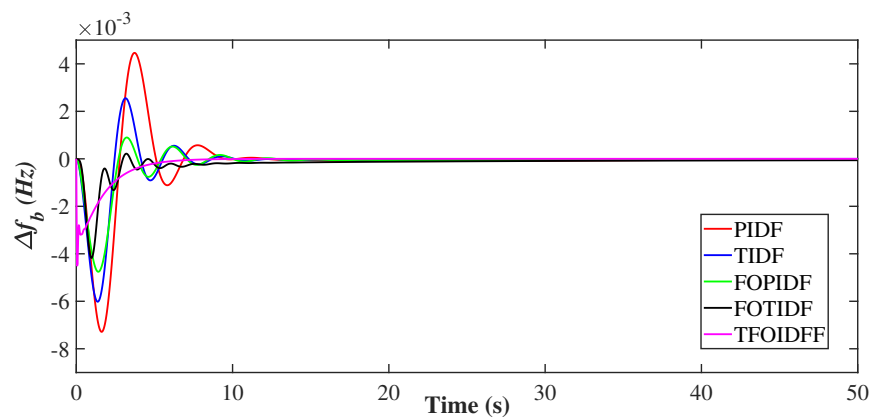
5.2. Scenario 2

In this scenario, the impact of inertia reduction on the interconnected multi-area power grid system is considered with the same SLP of the previous case, as the reduction of power grid system inertia can produce more frequency and voltage oscillations. Therefore, the multi-area power grid system inertia is reduced to 50% as an uncertainty situation in this case in order to investigate the performance of the new coordination of TFOIDFF and EVs in the LFC loop. Figure 14 shows that larger transient and more frequency fluctuations exist during the low system inertia condition than the previous case. It is clear that the proposed coordination of TFOIDFF LFC and EVs sharing based on the AHA technique can enhance

the dynamic frequency performance while diminishing the transient excursion with a fast response regarding disturbance refutation, tracking attribute, and minimum steady-state error compared with other controllers in this severe inertia condition. Furthermore, it can still maintain the frequency deviations within ± 0.003 Hz in both area a and area b with the lowest tie-line power deviation at 0.0004 p.u.
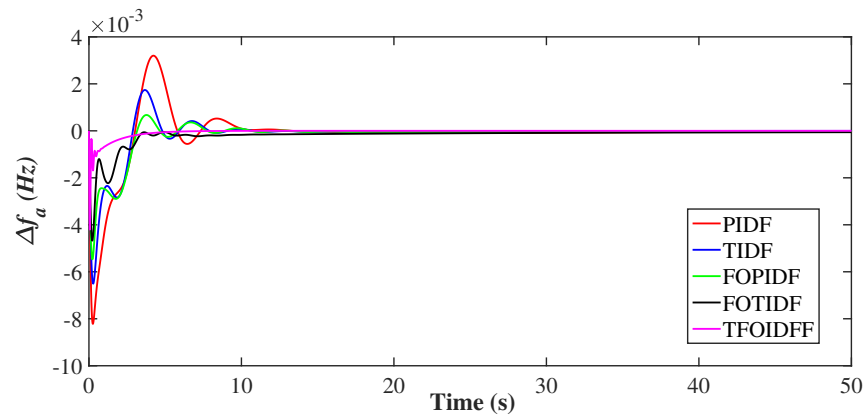

(a)

(b)
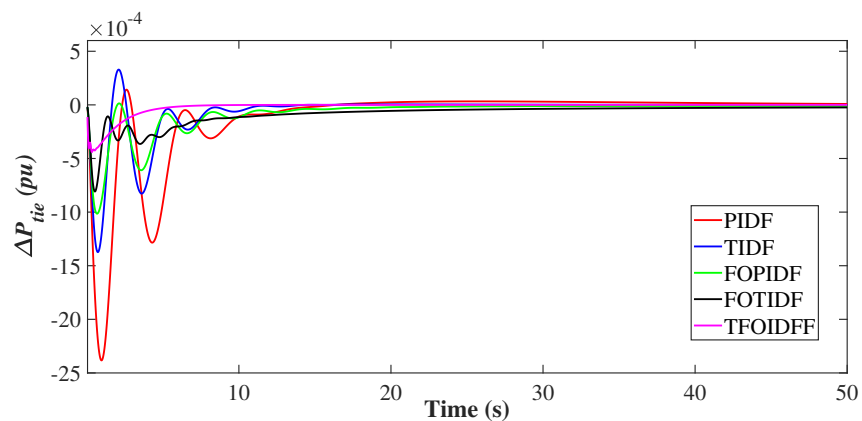
(c)

Figure 14. System responses in Scenario 2. (**a**) Δf_a; (**b**) Δf_b; (**c**) ΔP_{tie}.

The coordination of the FOTIDF comes in the second order as it can maintain the change in frequency at 0.0046 Hz in area a and 0.0044 in area b. Meanwhile, the FOPIDF comes thirdly by reducing the frequency fluctuations to 0.0054 Hz and 0.0048 Hz in the

two areas with a change in tie-line power at 0.001 p.u. Furthermore, the TIDF can dampen the frequency and power oscillation to 0.0065 Hz in area *a*, 0.006 Hz in area *b* and 0.0014 p.u tie-power deviation. However, the PIDF controllers come last in this comparison with frequency changes at 0.0082 Hz in area *a*, 0.0073 Hz in area *b*, and high tie-line deviation at 0.0024 p.u as summarized in Table 3. It can be concluded from this scenario that during the low system inertia condition, the designed LFC of TFOIDFF and power sharing from the EVs based on the AHA technique are more efficient in managing the abrupt load change and tracking the operating point of the multi-area power grid system.

5.3. Scenario 3

In this scenario, the studied two-area power grid system is tested against two-step in demand load, where, one of them is applied in area *a* of 10% at t = 0 s and the other SLP is 10% change in area *b* at t = 40 s under the default system parameters. The perturbed responses of frequency and power in areas *a* and *b* are depicted in Figure 15. It can be observed that the proposed TFOIDFF technique succeeded in maintaining the frequency and power deviations at the desired limits, which are lower than the other control techniques with fast and smooth performance in restoring the power grid system frequency and tie-line power as shown in Figure 15 and summarized in Table 3. Meanwhile, the worst performance was achieved by the PIDF controller as it shows around 0.0055 Hz change in frequency at initial time and 0.009 Hz at t = 40 s in area *a* and more than 0.014 Hz deviation at 40 s in area *b*.
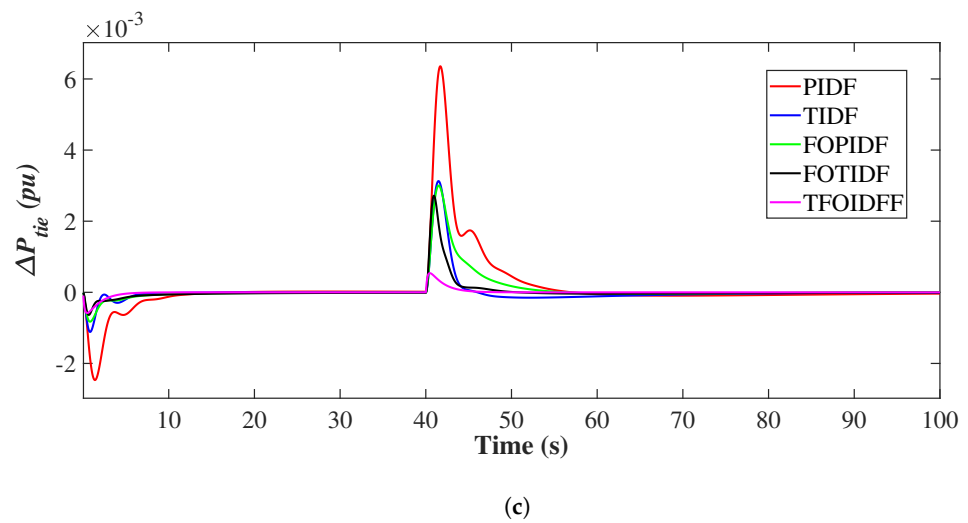

(a)

(b)

Figure 15. *Cont.*

(c)
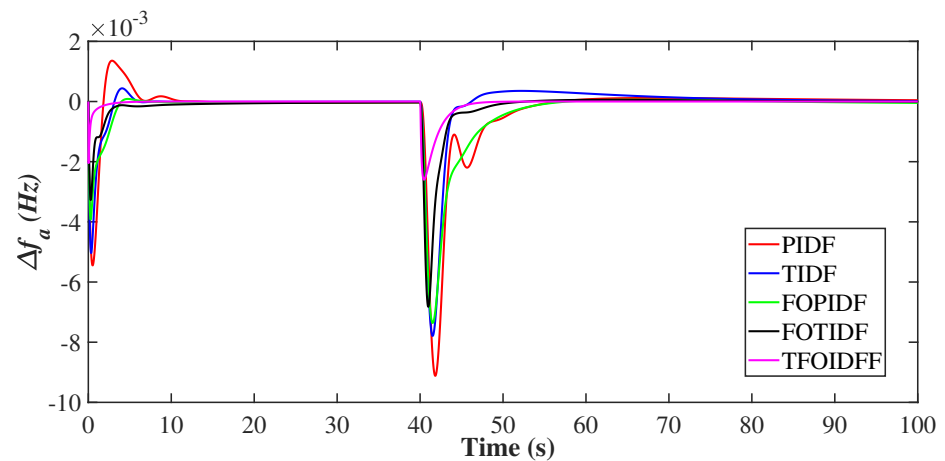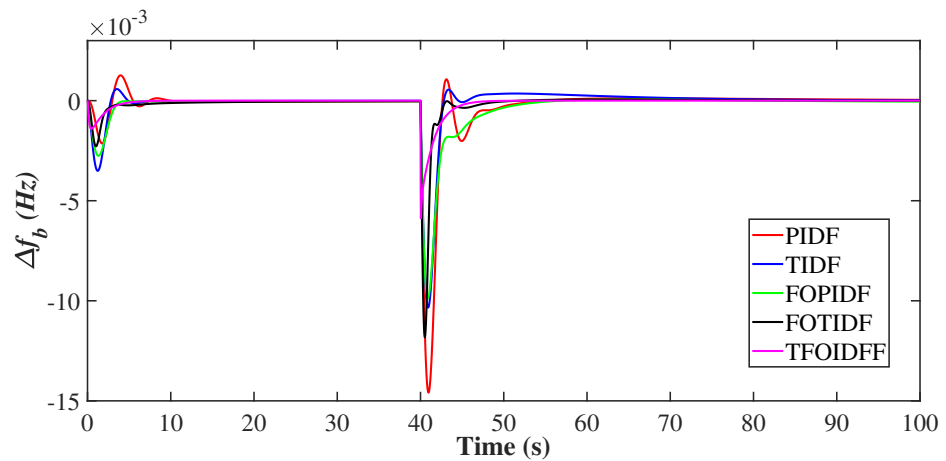
Figure 15. System responses in Scenario 3. (**a**) Δf_a; (**b**) Δf_b; (**c**) ΔP_{tie}.

The TIDF can slightly enhance these values to around a 0.0051 Hz change in frequency at initial time and 0.0077 Hz at t = 40 s in area *a* and more than 0.011 Hz deviation at 40 s in area *b*. However, the FOPIDF and FOTIDF can suppress the frequency and tie-line power oscillation to values better than those of PIDF and TIDF as noted in Table 3. Despite the impact of a sudden two-step load change in both areas during this case, the proposed coordination of optimized TFOIDFF LFC and the role of EVs as an auxiliary LFC based on the AHA technique still maintain the multi-area power grid system frequency within the acceptable range of standard control limits.

5.4. Scenario 4

In this case, the capability of the proposed coordination-based-LFC and EVs using the TFOIDFF controller based on the AHA method is evaluated and revealed under the impact of drastic multi-load change pattern as shown in Figure 16 of this scenario. Figure 17 shows the system frequency and power waveforms of the proposed multi-area power grid system during the impact of multi-step load variation. It is clear that dynamic responses of the proposed LFC strategy coordinated with the EV cooperation have faster actions with the least deviated values compared to other proposed control techniques. Wherein, it properly holds the frequency deviation within 0.015 Hz in area *a*, and 0.001 Hz in area *b* at time t = 80 s with fast and smooth settling time. Whereas, the other FOTIDF controller comes in the second order after the proposed one and gives frequency-deviated values of about 0.051 Hz in area *a*, and 0.022 Hz in area *b* with a deviation of 0.014 p.u in tie-line power as summarized in Table 3.
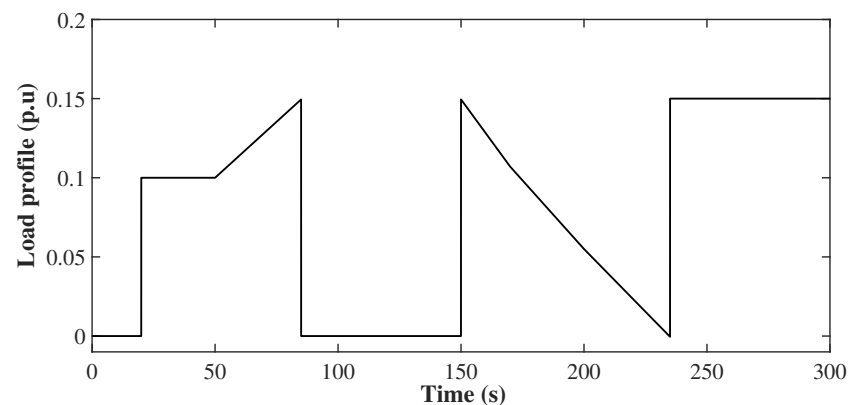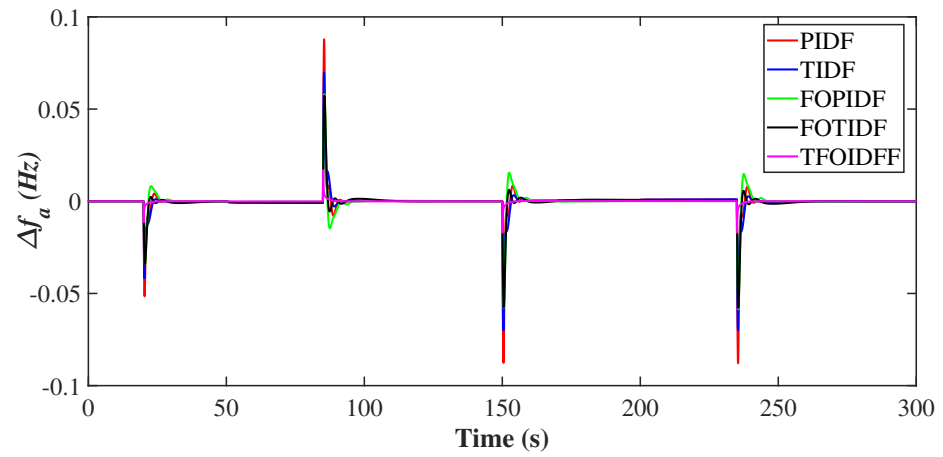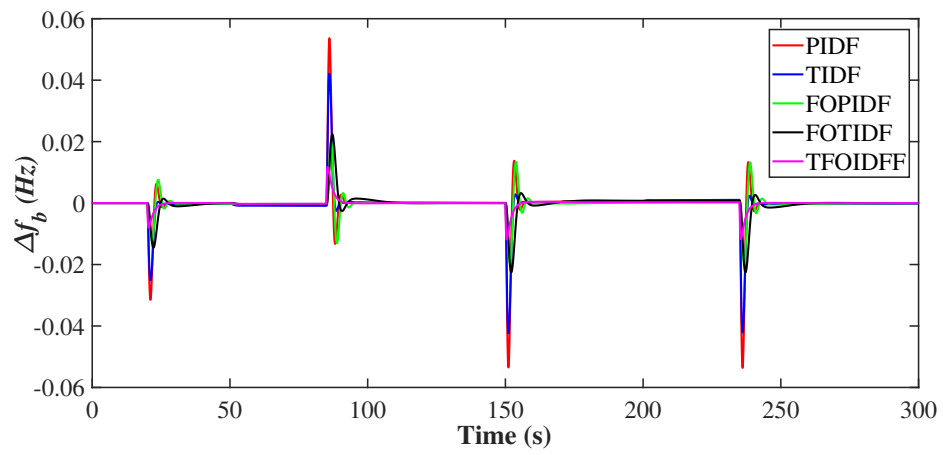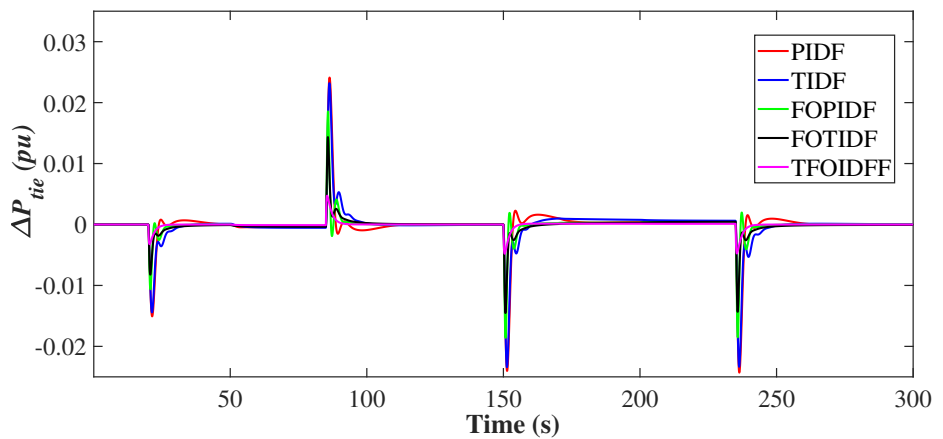

Figure 16. Loading profile for Scenario 4.

(a)

(b)

(c)

Figure 17. System responses in Scenario 4. (**a**) Δf_a; (**b**) Δf_b; (**c**) ΔP_{tie}.

The FOPIDF controller comes in the third order after TFOIDFF and FOTIDF controllers by maintaining the frequency at 0.058 Hz in area *a* and 0.02 Hz in area *b*. However, utilizing TIDF-based and PIDF-based controllers helps at restoring the system's frequency, and tie-line power-deviated values, but at the cost of longer settling times and high oscillations

of overshoot, and undershoot values of more than ±0.0.075 Hz, especially at instants of 80 s and 150 s for high-load variation instants.

5.5. Scenario 5

The main objective of this scenario is to demonstrate the performance of the studied multi-area power grid system with the proposed coordination of TFOIDFF and EV based on the new AHA technique under the impact of natural RES variations, which act as the main component of the actual power grid. However, the RESs lead to low-power system inertia due to existing inverter-based structures in power microgrid systems in addition to the absence of rotational masses. This, in turn, introduces several stability, reliability, and coordination issues for power grid operation. Therefore, the studied two-area power grid is examined by installing high-fluctuating PV and wind generation units as shown in Figure 18. In addition, a 10% SLP at t = 40 s of simulation is applied to area *a*, the PV generation is connected to the system at t = 0 s in area *b*, and the connection of wind unit is at t = 70 s in area *a*. The performance of all suggested controllers is evaluated in Figure 19.

It can be observed that, during the start of the system simulation, the first and second area frequency variations, along with the alteration in the tie-line power, increase temporarily in response to the surplus generation output from the PV integration at t = 0 s, especially with the conventional PIDF and TIDF controllers for frequency levels more than 0.07 Hz at 0 s and more than 0.1 Hz at the instant of wind generation insertion at 70 s in area *a*. In addition, more deviations exist in area *b* at around 0.1 Hz at 0 s and more than 0.08 Hz at t = 150 s for both controllers.
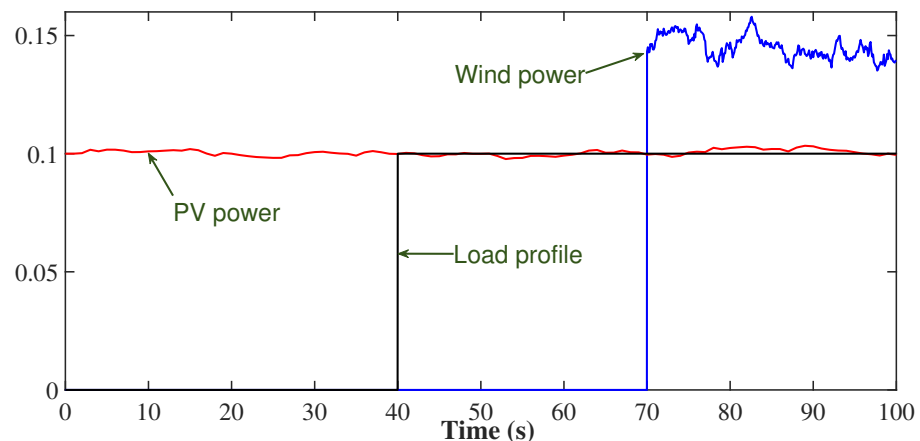

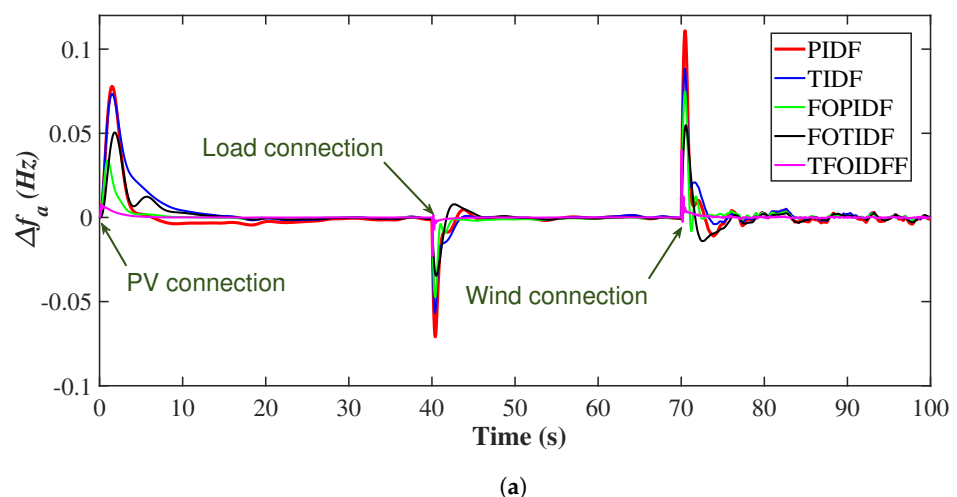
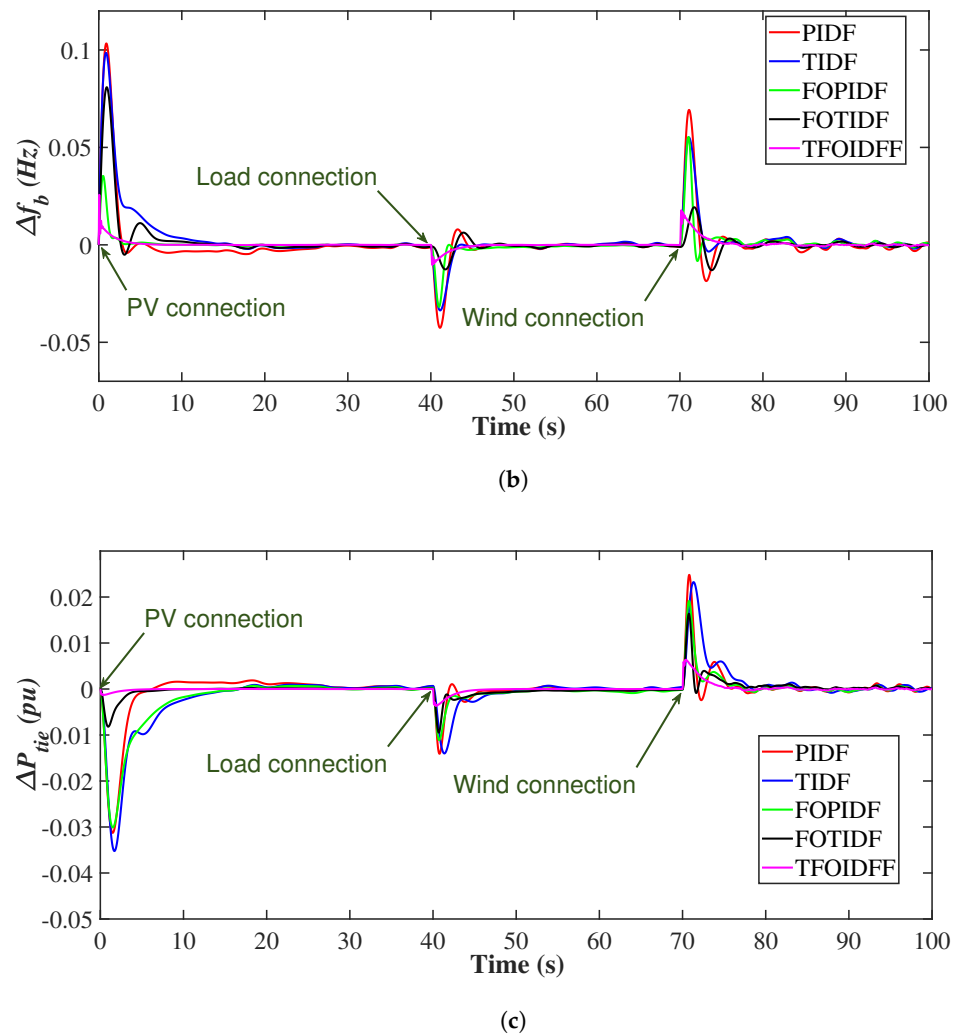**Figure 18.** Power profiles for Scenario 5.


(a)

Figure 19. *Cont.*

(b)

(c)

Figure 19. System responses in Scenario 5. (**a**) Δf_a; (**b**) Δf_b; (**c**) ΔP_{tie}.

Meanwhile, the FOPIDF controller can reduce deviation levels to nearly 0.05 Hz and 0.07 Hz in area *a* at 0 s and 70 s, respectively, and less than 0.07 Hz and 0.05 Hz in area *b* at the same instants of PV and wind power connection. Hence, the FOPIDF gives improved performance with better values than the PIDF and TIDF controllers. However, the FOTIDF and the proposed TFOIDFF are the most efficient and fastest techniques in restoring the power grid system frequency near its nominal value in both areas compared to other controllers in terms of overshoot, undershoot, settling time as summarized in Table 3.
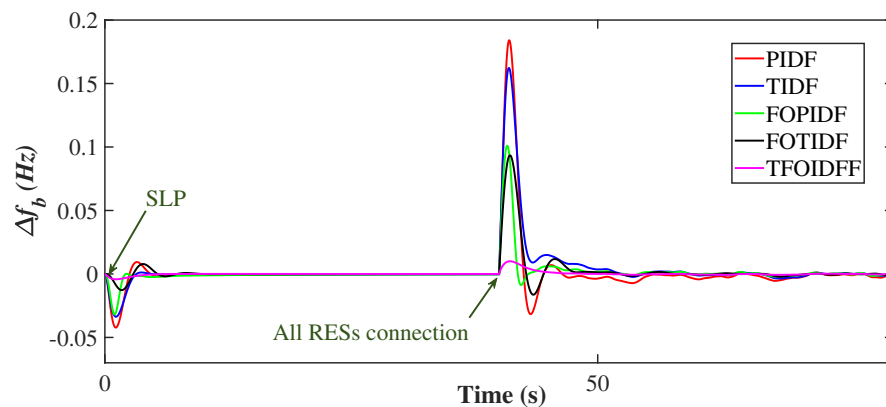
5.6. Scenario 6

This scenario considers further validation of the proposed TFOIDFF controller's performance under the impact of high penetration level of RESs. This case includes a 10% SLP at initial instant of simulation in addition to connecting all RESs at t = 40 s. Figure 20 shows the obtained performance comparisons of the proposed and suggested controllers. A high-oscillating frequency and tie-line power values can be observed to occur at the instant t = 40 s in this scenario due to the connection of all RESs at that time. It is clear from this figure that the highest deviations at this instant are achieved by the PIDF and TIDF controllers as they have frequency deviations at 0.15 Hz and 0.12 Hz in area *a*, respectively, and more than 0.18 Hz and 0.16 Hz in area *b* with tie-line power deviations at 0.03 p.u and 0.024 p.u, respectively. While the FOPIDF comes after them by reducing the frequency deviations to 0.1 Hz in both areas with a tie-line power of 0.016 p.u. at the same instant. When using the FOTIDF controller, the frequency deviation is maintained around 0.07 Hz

and 0.09 Hz in area *a* and area *b* at t = 40 s, respectively, with faster performance than the previous controllers. Meanwhile, the minimum overshoot/undershoot and settling time values are achieved by using the newly proposed TFOIDFF controller as summarized in Table 3. It can be concluded that for all the studied scenarios, the best performance of the interconnected power grid system can be achieved by applying the newly proposed TFOIDFF controller coordinated with the EV system in the LFC loop.
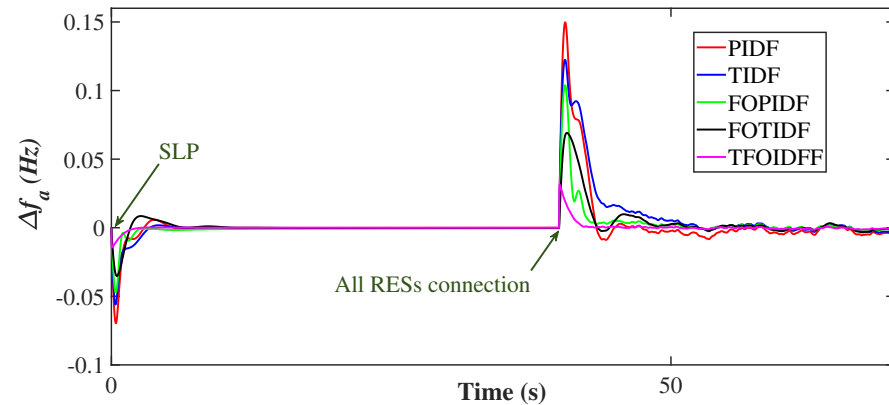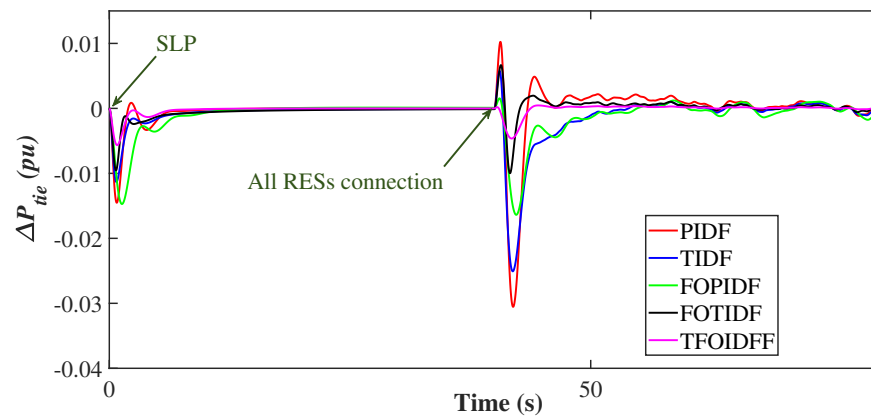
Figure 20. System responses in Scenario 6. (**a**) Δf_a; (**b**) Δf_b; (**c**) ΔP_{tie}.

6. Conclusions

A TFOIDFF controller representing a novel implementation combining the features of TID, FOPID, and fractional filter has been presented in this paper to enhance the LFC of a multi-area power grid system. In addition, the incorporation of mixed renewable generators and electrical vehicles are considered in this paper with fluctuations in RES generation and uncertainties in power system inertia. Moreover, a new application of the recently introduced AHA method is proposed for tuning the parameters of the new proposed TFOIDFF decentralized controller for the LFC and installed EVs in each area. The proposed TFOIDFF is validated against the existing non-linearities, uncertainties, and load/generation variations in the studied multi-area power grid system. Moreover, comprehensive comparisons of the new proposed TFOIDFF controller with LFC methods featured in the literature are presented in the paper. The obtained results verify the advantages of the proposed method as follows:

- The proposed TFOIDFF controller demonstrates a more efficient performance than the studied conventional PIDF and TIDF controllers, and the advanced FOPIDF and FOTIDF controllers.
- The obtained comparisons of ISE, ITSE, IAE, and ITAE objective functions verified the faster and better convergence of the proposed AHA method over the ABC, AEO, and BOA optimizers.
- Moreover, the obtained simulation results proved the minimized frequency, and tie-line power deviation using the proposed optimized TFOIDFF controller compared to existing LFC methods.
- Based on the designed optimized controllers, the coordination of the LFC and installed EVs is achieved to maintain multi-area power system stability during various existing disturbances in power systems.

Therefore, the proposed AHA-based optimized TFOIDFF controller can achieve enhanced performance in regulating the power grid system frequency. In addition, it can enhance the dynamical behavior of multi-area power grid systems with high-penetration levels of RESs, in consideration of potential future scenarios. Extension of this research work can be performed through extending the studied system (components and number of areas) to validate the proposed controller and optimization process. Moreover, the convergence behavior and objective function tracking can be studied in an interconnected power system with a larger number of areas.

Author Contributions: Conceptualization, E.A.M. and M.A.; Data curation, E.A.M., M.A. and M.W.; Formal analysis, E.A.M. and M.A.; Funding acquisition, M.W.; Investigation, E.A.M., M.A. and M.W.; Methodology, E.A.M., M.A. and M.W.; Project administration, M.W.; Resources, E.A.M. and M.A.; Software, E.A.M. and M.A.; Supervision, M.A. and M.W.; Validation, E.A.M., M.A. and M.W.; Visualization, E.A.M. and M.A.; Writing—original draft, E.A.M. and M.A.; Writing—review & editing, M.W. All authors have read and agreed to the published version of the manuscript.

Institutional Review Board Statement: Not applicable.

Informed Consent Statement: Not applicable.

Data Availability Statement: Not applicable.

Conflicts of Interest: The authors declare no conflict of interest.

References

1. Yildirim, B.; Gheisarnejad, M.; Khooban, M.H. A Robust Non-Integer Controller Design for Load Frequency Control in Modern Marine Power Grids. *IEEE Trans. Emerg. Top. Comput. Intell.* **2022**, *6*, 852–866. [CrossRef]
2. Ahmed, E.M.; Mohamed, E.A.; Elmelegi, A.; Aly, M.; Elbaksawi, O. Optimum Modified Fractional Order Controller for Future Electric Vehicles and Renewable Energy-Based Interconnected Power Systems. *IEEE Access* **2021**, *9*, 29993–30010. [CrossRef]

3. Sun, P.; Yun, T.; Chen, Z. Multi-objective robust optimization of multi-energy microgrid with waste treatment. *Renew. Energy* **2021**, *178*, 1198–1210. [CrossRef]
4. Xiao, D.; Chen, H.; Wei, C.; Bai, X. Statistical Measure for Risk-Seeking Stochastic Wind Power Offering Strategies in Electricity Markets. *J. Mod. Power Syst. Clean Energy* **2021**, [CrossRef]
5. Said, S.M.; Aly, M.; Hartmann, B.; Mohamed, E.A. Coordinated fuzzy logic-based virtual inertia controller and frequency relay scheme for reliable operation of low-inertia power system. *IET Renew. Power Gener.* **2021**, *15*, 1286–1300. [CrossRef]
6. Liu, L.; Hu, Z.; Mujeeb, A. Automatic Generation Control Considering Uncertainties of the Key Parameters in the Frequency Response Model. *IEEE Trans. Power Syst.* **2022**. [CrossRef]
7. Magdy, G.; Ali, H.; Xu, D. Effective control of smart hybrid power systems: Cooperation of robust LFC and virtual inertia control system. *CSEE J. Power Energy Syst.* **2021**. [CrossRef]
8. Paliwal, N.; Srivastava, L.; Pandit, M. Application of grey wolf optimization algorithm for load frequency control in multi-source single area power system. *Evol. Intell.* **2020**, *15*, 563–584. [CrossRef]
9. Aryan, P.; Ranjan, M.; Shankar, R. Deregulated LFC scheme using equilibrium optimized Type-2 fuzzy controller. *WEENTECH Proc. Energy* **2021**, *8*, 494–505. [CrossRef]
10. Dreidy, M.; Mokhlis, H.; Mekhilef, S. Inertia response and frequency control techniques for renewable energy sources: A review. *Renew. Sustain. Energy Rev.* **2017**, *69*, 144–155. [CrossRef]
11. Fernández-Guillamón, A.; Gómez-Lázaro, E.; Muljadi, E.; Molina-García, Á. Power systems with high renewable energy sources: A review of inertia and frequency control strategies over time. *Renew. Sustain. Energy Rev.* **2019**, *115*, 109369. [CrossRef]
12. Lv, X.; Sun, Y.; Wang, Y.; Dinavahi, V. Adaptive Event-Triggered Load Frequency Control of Multi-Area Power Systems Under Networked Environment via Sliding Mode Control. *IEEE Access* **2020**, *8*, 86585–86594. [CrossRef]
13. Vrdoljak, K.; Perić, N.; Petrović, I. Sliding mode based load-frequency control in power systems. *Electr. Power Syst. Res.* **2010**, *80*, 514–527. [CrossRef]
14. Pan, C.; Liaw, C. An adaptive controller for power system load-frequency control. *IEEE Trans. Power Syst.* **1989**, *4*, 122–128. [CrossRef]
15. Bu, X.; Yu, W.; Cui, L.; Hou, Z.; Chen, Z. Event-Triggered Data-Driven Load Frequency Control for Multiarea Power Systems. *IEEE Trans. Ind. Inform.* **2022**, *18*, 5982–5991. [CrossRef]
16. Xiaofeng Yu.; Tomsovic, K. Application of linear matrix inequalities for load frequency control with communication delays. *IEEE Trans. Power Syst.* **2004**, *19*, 1508–1515. [CrossRef]
17. Rakhshani, E.; Rodriguez, P.; Cantarellas, A.M.; Remon, D. Analysis of derivative control based virtual inertia in multi-area high-voltage direct current interconnected power systems. *IET Gener. Transm. Distrib.* **2016**, *10*, 1458–1469. [CrossRef]
18. Kerdphol, T.; Rahman, F.S.; Mitani, Y.; Watanabe, M.; Kufeoglu, S. Robust Virtual Inertia Control of an Islanded Microgrid Considering High Penetration of Renewable Energy. *IEEE Access* **2018**, *6*, 625–636. [CrossRef]
19. Li, X.; Ye, D. Event-Based Distributed Fuzzy Load Frequency Control for Multiarea Nonlinear Power Systems with Switching Topology. *IEEE Trans. Fuzzy Syst.* **2022**. [CrossRef]
20. Saxena, S.; Hote, Y.V. Load Frequency Control in Power Systems via Internal Model Control Scheme and Model-Order Reduction. *IEEE Trans. Power Syst.* **2013**, *28*, 2749–2757. [CrossRef]
21. İlhan Kocaarslan.; Çam, E. Fuzzy logic controller in interconnected electrical power systems for load-frequency control. *Int. J. Electr. Power Energy Syst.* **2005**, *27*, 542–549. [CrossRef]
22. Shiroei, M.; Ranjbar, A. Supervisory predictive control of power system load frequency control. *Int. J. Electr. Power Energy Syst.* **2014**, *61*, 70–80. [CrossRef]
23. Pandey, S.K.; Mohanty, S.R.; Kishor, N. A literature survey on load–frequency control for conventional and distribution generation power systems. *Renew. Sustain. Energy Rev.* **2013**, *25*, 318–334. [CrossRef]
24. Shankar, R.; Pradhan, S.; Chatterjee, K.; Mandal, R. A comprehensive state of the art literature survey on LFC mechanism for power system. *Renew. Sustain. Energy Rev.* **2017**, *76*, 1185–1207. [CrossRef]
25. Panda, S.; Mohanty, B.; Hota, P. Hybrid BFOA-PSO algorithm for automatic generation control of linear and nonlinear interconnected power systems. *Appl. Soft Comput.* **2013**, *13*, 4718–4730. [CrossRef]
26. Khokhar, B.; Dahiya, S.; Singh Parmar, K.P. Atom search optimization based study of frequency deviation response of a hybrid power system. In Proceedings of the 2020 IEEE 9th Power India International Conference (PIICON), Sonepat, India, 28 February–1 March 2020; pp. 1–5. [CrossRef]
27. Sharma, J.; Hote, Y.V.; Prasad, R. PID controller design for interval load frequency control system with communication time delay. *Control. Eng. Pract.* **2019**, *89*, 154–168. [CrossRef]
28. El Yakine Kouba, N.; Menaa, M.; Hasni, M.; Boudour, M. Optimal load frequency control based on artificial bee colony optimization applied to single, two and multi-area interconnected power systems. In Proceedings of the 2015 3rd International Conference on Control, Engineering & Information Technology (CEIT), Tlemcen, Algeri, 25–27 May 2015; pp. 1–6. [CrossRef]
29. Yousri, D.; Babu, T.S.; Fathy, A. Recent methodology based Harris Hawks optimizer for designing load frequency control incorporated in multi-interconnected renewable energy plants. *Sustain. Energy Grids Netw.* **2020**, *22*, 100352. [CrossRef]
30. Dahab, Y.A.; Abubakr, H.; Mohamed, T.H. Adaptive Load Frequency Control of Power Systems Using Electro-Search Optimization Supported by the Balloon Effect. *IEEE Access* **2020**, *8*, 7408–7422. [CrossRef]

31. Shiva, C.; Shankar, G.; Mukherjee, V. Automatic generation control of power system using a novel quasi-oppositional harmony search algorithm. *Int. J. Electr. Power Energy Syst.* **2015**, *73*, 787–804. [CrossRef]
32. Mohanty, B.; Panda, S.; Hota, P.K. Controller parameters tuning of differential evolution algorithm and its application to load frequency control of multi-source power system. *Int. J. Electr. Power Energy Syst.* **2014**, *54*, 77–85. [CrossRef]
33. Sahu, R.; Panda, S.; Rout, U.K.; Sahoo, D. Teaching learning based optimization algorithm for automatic generation control of power system using 2-DOF PID controller. *Int. J. Electr. Power Energy Syst.* **2016**, *77*, 287–301. [CrossRef]
34. Dash, P.; Saikia, L.; Sinha, N. Automatic generation control of multi area thermal system using Bat algorithm optimized PD–PID cascade controller. *Int. J. Electr. Power Energy Syst.* **2015**, *68*, 364–372. [CrossRef]
35. Raju, M.; Saikia, L.; Sinha, N. Automatic generation control of a multi-area system using ant lion optimizer algorithm based PID plus second order derivative controller. *Int. J. Electr. Power Energy Syst.* **2016**, *80*, 52–63. [CrossRef]
36. Gheisarnejad, M. An effective hybrid harmony search and cuckoo optimization algorithm based fuzzy PID controller for load frequency control. *Appl. Soft Comput.* **2018**, *65*, 121–138. [CrossRef]
37. Prakash, S.; Sinha, S. Simulation based neuro-fuzzy hybrid intelligent PI control approach in four-area load frequency control of interconnected power system. *Appl. Soft Comput.* **2014**, *23*, 152–164. [CrossRef]
38. Latif, A.; Paul, M.; Das, D.C.; Hussain, S.M.S.; Ustun, T.S. Price Based Demand Response for Optimal Frequency Stabilization in ORC Solar Thermal Based Isolated Hybrid Microgrid under Salp Swarm Technique. *Electronics* **2020**, *9*, 2209. [CrossRef]
39. Hussain, I.; Das, D.C.; Latif, A.; Sinha, N.; Hussain, S.S.; Ustun, T.S. Active power control of autonomous hybrid power system using two degree of freedom PID controller. *Energy Rep.* **2022**, *8*, 973–981. [CrossRef]
40. Delassi, A.; Arif, S.; Mokrani, L. Load frequency control problem in interconnected power systems using robust fractional PI λ D controller. *Ain Shams Eng. J.* **2018**, *9*, 77–88. [CrossRef]
41. Fathy, A.; Alharbi, A.G. Recent Approach Based Movable Damped Wave Algorithm for Designing Fractional-Order PID Load Frequency Control Installed in Multi-Interconnected Plants With Renewable Energy. *IEEE Access* **2021**, *9*, 71072–71089. [CrossRef]
42. Ayas, M.S.; Sahin, E. FOPID controller with fractional filter for an automatic voltage regulator. *Comput. Electr. Eng.* **2021**, *90*, 106895. [CrossRef]
43. Arya, Y.; Kumar, N.; Dahiya, P.; Sharma, G.; Çelik, E.; Dhundhara, S.; Sharma, M. Cascade-$I^\lambda D^\mu N$ controller design for AGC of thermal and hydro-thermal power systems integrated with renewable energy sources. *IET Renew. Power Gener.* **2021**, *15*, 504–520. [CrossRef]
44. Oshnoei, S.; Oshnoei, A.; Mosallanejad, A.; Haghjoo, F. Contribution of GCSC to regulate the frequency in multi-area power systems considering time delays: A new control outline based on fractional order controllers. *Int. J. Electr. Power Energy Syst.* **2020**, *123*, 106197. [CrossRef]
45. Oshnoei, A.; Khezri, R.; Muyeen, S.M.; Oshnoei, S.; Blaabjerg, F. Automatic Generation Control Incorporating Electric Vehicles. *Electr. Power Components Syst.* **2019**, *47*, 720–732. [CrossRef]
46. Priyadarshani, S.; Subhashini, K.R.; Satapathy, J.K. Pathfinder algorithm optimized fractional order tilt-integral-derivative (FOTID) controller for automatic generation control of multi-source power system. *Microsyst. Technol.* **2020**, *27*, 23–35. [CrossRef]
47. Sahu, R.K.; Panda, S.; Biswal, A.; Sekhar, G.C. Design and analysis of tilt integral derivative controller with filter for load frequency control of multi-area interconnected power systems. *ISA Trans.* **2016**, *61*, 251–264. [CrossRef] [PubMed]
48. Malik, S.; Suhag, S. A Novel SSA Tuned PI-TDF Control Scheme for Mitigation of Frequency Excursions in Hybrid Power System. *Smart Sci.* **2020**, *8*, 202–218. [CrossRef]
49. Latif, A.; Hussain, S.M.S.; Das, D.C.; Ustun, T.S. Optimum Synthesis of a BOA Optimized Novel Dual-Stage PI $-$ (1 + ID) Controller for Frequency Response of a Microgrid. *Energies* **2020**, *13*, 3446. [CrossRef]
50. Mohamed, E.A.; Ahmed, E.M.; Elmelegi, A.; Aly, M.; Elbaksawi, O.; Mohamed, A.A.A. An Optimized Hybrid Fractional Order Controller for Frequency Regulation in Multi-area Power Systems. *IEEE Access* **2020**, *8*, 213899–213915. [CrossRef]
51. Arya, Y. A novel CFFOPI-FOPID controller for AGC performance enhancement of single and multi-area electric power systems. *ISA Trans.* **2020**, *100*, 126–135. [CrossRef]
52. Arya, Y. A new optimized fuzzy FOPI-FOPD controller for automatic generation control of electric power systems. *J. Frankl. Inst.* **2019**, *356*, 5611–5629. [CrossRef]
53. Gheisarnejad, M.; Khooban, M.H. Design an optimal fuzzy fractional proportional integral derivative controller with derivative filter for load frequency control in power systems. *Trans. Inst. Meas. Control* **2019**, *41*, 2563–2581. [CrossRef]
54. Arya, Y. Improvement in automatic generation control of two-area electric power systems via a new fuzzy aided optimal PIDN-FOI controller. *ISA Trans.* **2018**, *80*, 475–490. [CrossRef] [PubMed]
55. Khamies, M.; Magdy, G.; Selim, A.; Kamel, S. An improved Rao algorithm for frequency stability enhancement of nonlinear power system interconnected by AC/DC links with high renewables penetration. *Neural Comput. Appl.* **2021**, *34*, 2883–2911. [CrossRef]
56. Elkasem, A.H.A.; Kamel, S.; Hassan, M.H.; Khamies, M.; Ahmed, E.M. An Eagle Strategy Arithmetic Optimization Algorithm for Frequency Stability Enhancement Considering High Renewable Power Penetration and Time-Varying Load. *Mathematics* **2022**, *10*, 854. [CrossRef]
57. Zhao, W.; Wang, L.; Mirjalili, S. Artificial hummingbird algorithm: A new bio-inspired optimizer with its engineering applications. *Comput. Methods Appl. Mech. Eng.* **2022**, *388*, 114194. [CrossRef]

58. Ramadan, A.; Ebeed, M.; Kamel, S.; Ahmed, E.M.; Tostado-Véliz, M. Optimal allocation of renewable DGs using artificial hummingbird algorithm under uncertainty conditions. *Ain Shams Eng. J.* **2022**, *2022*, 101872. [CrossRef]

59. Alamir, N.; Kamel, S.; Megahed, T.F.; Hori, M.; Abdelkader, S.M. Developing an Artificial Hummingbird Algorithm for Probabilistic Energy Management of Microgrids Considering Demand Response. *Front. Energy Res.* **2022**, *10*, 876. [CrossRef]

60. Falahati, S.; Taher, S.A.; Shahidehpour, M. Grid Secondary Frequency Control by Optimized Fuzzy Control of Electric Vehicles. *IEEE Trans. Smart Grid* **2018**, *9*, 5613–5621. [CrossRef]

61. Luo, X.; Xia, S.; Chan, K.W. A decentralized charging control strategy for plug-in electric vehicles to mitigate wind farm intermittency and enhance frequency regulation. *J. Power Sources* **2014**, *248*, 604–614. [CrossRef]

62. Ota, Y.; Taniguchi, H.; Nakajima, T.; Liyanage, K.M.; Baba, J.; Yokoyama, A. Autonomous Distributed V2G (Vehicle-to-Grid) Satisfying Scheduled Charging. *IEEE Trans. Smart Grid* **2012**, *3*, 559–564. [CrossRef]

63. Falahati, S.; Taher, S.A.; Shahidehpour, M. A new smart charging method for EVs for frequency control of smart grid. *Int. J. Electr. Power Energy Syst.* **2016**, *83*, 458–469. [CrossRef]

64. Ray, P.K.; Mohanty, S.R.; Kishor, N. Proportional–integral controller based small-signal analysis of hybrid distributed generation systems. *Energy Convers. Manag.* **2011**, *52*, 1943–1954. [CrossRef]

65. Abraham, R.J.; Das, D.; Patra, A. Automatic generation control of an interconnected hydrothermal power system considering superconducting magnetic energy storage. *Int. J. Electr. Power Energy Syst.* **2007**, *29*, 571–579. [CrossRef]

66. Micev, M.; Ćalasan, M.; Oliva, D. Fractional Order PID Controller Design for an AVR System Using Chaotic Yellow Saddle Goatfish Algorithm. *Mathematics* **2020**, *8*, 1182. [CrossRef]

67. Dulf, E.H. Simplified Fractional Order Controller Design Algorithm. *Mathematics* **2019**, *7*, 1166. [CrossRef]

68. Motorga, R.; Mureșan, V.; Unguresan, M.L.; Abrudean, M.; Vălean, H.; Clitan, I. Artificial Intelligence in Fractional-Order Systems Approximation with High Performances: Application in Modelling of an Isotopic Separation Process. *Mathematics* **2022**, *10*, 1459. [CrossRef]

69. Tejado, I.; Vinagre, B.; Traver, J.; Prieto-Arranz, J.; Nuevo-Gallardo, C. Back to Basics: Meaning of the Parameters of Fractional Order PID Controllers. *Mathematics* **2019**, *7*, 530. [CrossRef]

70. Mihaly, V.; Şuşcă, M.; Dulf, E.H. μ-Synthesis FO-PID for Twin Rotor Aerodynamic System. *Mathematics* **2021**, *9*, 2504. [CrossRef]

71. Fathy, A. A novel artificial hummingbird algorithm for integrating renewable based biomass distributed generators in radial distribution systems. *Appl. Energy* **2022**, *323*, 119605. [CrossRef]